Geologic Mapping in the Afar with Landsat 7 ETM+ Data

Michael G. Bagley
Senior Integrative Exercise
March 9, 2005

Submitted in partial fulfillment of the requirements for a Bachelor of Arts degree from
Carleton College, Northfield, Minnesota

Geologic mapping with Landsat 7 data in the Afar

Michael Bagley
Senior Integrative Exercise
March 9, 2005

Bereket Haileab, Advisor

Abstract
This study reviews the utility of image enhancement techniques implemented on Landsat 7 Enhanced Thematic Mapper (ETM+) data with industry-standard remote sensing software for geologically useful mapping in the Awash region of the Afar. Detailed geologic maps for this area are difficult to acquire for ground-truthing of lithologic units, and thus it was the aim of this study to produce high-resolution images that would be as useful as possible for guiding future field work in the area. Image ratioing, IHS enhancement, and PC decorellation were used to create images in which the Pleistocene to Holocene lava flows, tuffs, and sediments could be interpreted visually, then classified into distinct units by mostly automated means.

Keywords: Afar, Landsat, reflectivity, remote sensing, spectra, spectral analysis

Table of Contents

Introduction

A field geologist aspiring to study the Afar Valley in northeastern Africa can encounter a huge variety of practical hurdles. Travel to the general region is time consuming and expensive, and transportation within the Afar is difficult and possibly dangerous due to the heat (up to 38ºC, <100mm rain per year), limited road systems and political upheaval (Getahun, 2003). Satellites, properly utilized, can provide as much or more information than a field excursion, while the investigator remains in the comfort of an air-conditioned office. Not only that, but they can survey an area orders of magnitude larger than is possible in any ground investigation, with no interference from rugged terrain or political barriers. Clearly, remote sensing provides an opportunity for huge time and money savings (Table 1) (Drury, 2001).

This opportunity has been exploited by many investigators, although few have chosen to work in the Afar. There has been a PhD proposal published on Landsat 7 Enhanced Thematic Mapper (ETM+) applications in the Afar, but it is unclear in the literature whether it was completed (Mengesha, 2000). Erta'Ale volcano in the northern Afar has been studied in detail by satellite to investigate its thermal flux and discharge from 1965 to 1996 (Oppenheimer and Francis, 1997). The extent of pumice deposits and sub-tephric lava flows surrounding Dubbi volcano, in the northeastern Afar, were measured with Landsat Thematic Mapper (TM) and Synthetic Aperture Radar (SAR) in order to study the only recorded explosive volcanic eruption in the Afar, in 1851, and evaluate the possibility for dangerous future eruptions (Wiart et al., 2000). Parts of the Kenyan Rift Valley and the Southern Red Sea Hills of Sudan have been mapped with

Landsat TM data in order to enhance existing geologic maps (Jutz and Chorowicz, 1993; Kenea, 1997).

Little else has been done with remote sensing in the Afar region. However, there has been a lot of work done in other areas of the world that has general applications. In particular, one group of investigators did some work on Landsat TM and SPOT panchromatic image merging in Brittany, France, and its applications for geologic mapping, that I applied to mapping in the Afar (Yesou et al., 1993). A study in Cuprite, Nevada with Advanced Spaceborne Thermal Emission and Reflection Radiometer (ASTER) data established that remote sensing has the potential to produce field-quality map products (Abrams and Hook, 1995).

In my study, I investigate Landsat 7 ETM+ data processed with various image enhancement methods, and its application for useful geologic mapping in Middle Awash region of the Afar Rift Valley. This is a particularly well-suited location for remote sensing analysis for a variety of reasons. As mentioned before, it is quite remote (the nearest airport is in Addis Ababa, 325km away by road), very hot, and very dry (Getahun, 2003). The aridity of the environment implies that there is little vegetation to obscure rock and soil surfaces from orbital view. The area is extremely significant in the fields of both igneous petrology, as the spreading center of three tectonic plates, and paleoanthropology, as the site of Pliocene to Pleistocene hominid fossils (Winter, 2001; WoldeGabriel et al., 2000).

Characteristics of Image Data

The information our eyes interpret as the "color" of a material is essentially determined by certain chemical characteristics of that material's surface; various chemical bonds absorb characteristic wavelengths and reflect most others. This means that color, and its equivalent in infrared wavelengths, can be exploited to map variations in chemical composition even from 705km away, with the aid of a conveniently located multispectral scanning radiometer such as the ETM+ (Enhanced Thematic Mapper) carried by Landsat 7. ETM+ sees a terrain's "colors" as the relative intensities of the light received in the eight bands (wavelengths) it is equipped to measure. If one takes these relative intensities for a given pixel (the smallest spatial unit of discrete information) and plots them on a graph, you have essentially mapped its spectrum of absorption and reflectance. Comparing this spectrum to a set of spectra that you have measured in the lab for a wide array of minerals (Ramasamy et al., 1993) can be the basis for a highly quantitative and precise geologic map.

Unfortunately, this approach follows the assumption that every material has an individual and distinguishable spectrum. This is true; every material does have a characteristic spectrum that can be used as a "fingerprint" for its identification. However, the relatively coarse resolution of ETM+ data introduces two important limiting factors to the extent of spectral mapping that is possible with the Landsat 7 platform: spatial resolution (which can potentially be circumvented with appropriate mathematics), and wavelength resolution (which cannot).

Spatial resolution limits spectral mapping in a fairly obvious way. Each pixel of ETM+ data represents a 30x30m section of terrain. Clearly, these squares of land are not likely to be homogenous in composition. Therefore, the wavelengths of light reflected or emitted by all the different materials in a given 30x30m square will be mixed together in the information provided by the resultant pixel of Landsat 7 data. Clearly, this is a hindrance to matching the spectrum from this pixel to that of a pure sample of some mineral. It is likely that the spectrum such a "mixed" pixel (as opposed to a hypothetical "pure" pixel of a spectrally homogenous area) will contain elements with overlapping absorption bands. However, Fourier analysis and related mathematical techniques can theoretically be employed to "un-mix" the data inherent in mixed pixels (Cloutis, 1996).

A much greater hindrance to accurate remote spectral mapping is that of wavelength resolution. In the field of modern remote spectroscopy, platforms such as Landsat 7 are now considered broadband to the point of being nearly useless. The number and width of the bands detected by a sensor define its spectral resolution. The data-gathering characteristics described in Table 2, for instance, define the extent of the spectral resolution of the ETM+ instrument. The six bands of sufficiently small wavelength range for spectral mapping (bands 6 and 8 collect information in a wide range of wavelengths for mapping purely thermal and spatial characteristics, respectively, at resolutions of 120m and 15m) are a highly limiting factor to defining a characteristic spectrum for even the most spectrally pure pixel. The absorption/reflectance spectrum one can create has only those six points of data, between which one can only linearly interpolate to create a coarse spectrum.

Table 1. Estimated efficiency for different methods of geologic mapping (Modified from Drury, 2001)

Methods	Cost	Efficiency (km/day)
Preliminaries		
Satellite remote sensing	0.02	>10^6
Interpretation and map	0.7	10^4
Airborne remote sensing	10	500
Interpretation and map	5	50
Airborne geophysics		500
Magnetic and electromagnetic	25	25
Interpretation and map	10	-
Literature search	250 $/day	
Field studies		
Geological reconnaissance	160	10
Detailed geological mapping	600	1
Geochemical surveying orientation	15	50
Drainage survey	50	25
Soil or biogeochemical survey	750	2
Geophysical surveying		
Resistivity and spontaneous potential	160 $/km	10
Induced potential	5000 $/km	0.5
Diamond drill cores	40 $/m	-
Shaft sinking	5000 $/m	-

Table 2. Spectral and spatial resolutions of Landsat 7 ETM+ bands (Modified from NASA, 2005)

Band	Wavelength Range	Resolution (m)
1	0.45-0.52	28.5
2	0.52-0.60	28.5
3	0.63-0.69	28.5
4	0.76-0.90	28.5
5	7.55-1.75	28.5
6	10.4-12.5	57
7	2.08-2.35	28.5
8	0.52-0.90	14.5

In consequence of this coarseness, if a material happens to have an absorption band that forms a particularly narrow section of a given band, it may be overwhelmed in the final pixel's information by high reflectance in the rest of the rather wide range of wavelengths actually sensed for each single band by the observing instrument. A narrow absorption band could also fall somewhere between the bandwidths covered, and thus be entirely undetected. Coarse bandwidth is particularly problematic at infrared wavelengths, where most of the useful spectral information is found for mineral reflectance spectrometry, and this is a problem that cannot be worked around in mapping with Landsat 7 data.

There do exist so-called hyperspectral sensing platforms that obtain high enough spectral resolutions that stunningly accurate compositional maps can be produced, sometimes with higher accuracies than those produced by conventional field observation (Abrams and Hook, 1995).NASA/JPL's AVIRIS (Airborne Visible/Infrared Imaging Spectrometer), for instance, measures EM radiation in 224 contiguous bands from 0.4-2.5μm, a spectral resolution over thirty-seven times that of Landsat 7 (Cloutis, 1996). Unfortunately, hyperspectral data is currently only generated by aircraft-based platforms like AVIRIS, which do not currently perform measurements in northeastern Africa.

The spectral and spatial resolution limitations of Landsat 7 data serve to define the boundaries of what is possible in its use for geological mapping. However, the infeasibility of ground-inspection-grade lithologic mapping does not preclude useful information from being extracted from this data. It simply means that it is mostly only possible to map general lithologic units, and to accept a high degree of compositional uncertainty. Maps derived from Landsat data should ultimately be supported by ground-

truthing for increased accuracy. In some ways, this lack of detail is probably better for producing useful geological maps, as it forces concentration on the big picture and look into a variety of image manipulation techniques in order to extract as much information as possible. Thus, my project focuses on a variety of different methods in an attempt to map useful lithologic units and structural elements in the Afar, always with the caveat in mind that none of it can be compositionally certain or detailed without hyperspectral or ground-truth data. Fortunately, even if no compositional data whatsoever could be extracted from the image data, simple textural and stratigraphic clues would still be very useful for mapping and interpretation.

Geologic Setting

The Afar Triangle can be geographically defined as the area enclosed by the Ethiopian Highland to the west, the Somali Plateau in the south, and the Danakil Horst to the east. This area has been under modern geological scrutiny for at least a century, as one of the few continental triple junctions on Earth (Bowen and Jux, 1987). The Afar is a rift valley at the origin of a rift system extending at least 2000km to the south, at the northern termination of the Eastern Rift's 4-80km wide graben system. It is thought to be the convergence point of three major tectonic spreading systems, at which the Arabian Plate, Nubian Plate, and Somalian Plate are all moving away from one another. Additionally, geophysical work indicates a low-velocity zone (associated with zones of hotter material) beneath parts of the two major rifting systems to the south (Winter, 2001). These rift systems are thought to have initiated around 15Ma ago, and evidence of volcanism exists from that time period to the present.

Most exposed surfaces in my study area are likely to be either possibly rift-associated extrusive volcanics ranging in age from Miocene to Holocene, non-rift-associated extrusive volcanics of older ages (Pallister, 1968), or post-volcanic sediments, ash and tuffs (Jutz and Chorowicz, 1993).

Sediments interbedded with Late Miocene to Pleistocene rift lavas are either fluvial, overbank, or lacustrine, and highly fossiliferous (Renne et al., 1999). The Middle Awash area is also well-known for its hominid fossils, which are primarily found in the Pliocene volcaniclastic sediments related to the development of the rift basin in the late Miocene (WoldeGabriel et al., 2000). Older sediments do not seem to exist in the Afar, apparently due to its rapid erosional and depositional cycles, which have covered or disposed of the fossil record of the late Miocene (WoldeGabriel et al., 2000). The presence of hominid fossils (the "Lucy" species, among others) in the tuffaceous sediments of the Afar also makes it one of the most important paleoanthropological sites in the world.

Methods

Data Acquisition

All Landsat data to date has been collected, pre-processed for image format compatibility, and made available free of charge (GLCF, 2005; USGS, 2005). The USGS maintains one useful online interface for acquiring data, as does the Global Land Cover Facility (GLCF). This project is sponsored by the University of Maryland, NASA, Raytheon Corporation, and the United Nations (GLCF, 2005). At least 40 full-resolution ETM+ and SRTM images from GLCF were used over the course of this project. The full

ETM+ data set for a given unit of land area (a "scene") is actually at least eight 12-240MB image files, one for each wavelength band, each of which is at least 60MB. I decided to concentrate on a Landsat scene in the Awash centered at N10.1289º, E41.0684º. This scene is approximately rhombus-shaped, as are all Landsat images, and covers ~33,704Km^2.

Initial Processing

Initial evaluation of data took place with Purdue University's MultiSpec. However, this program's capability for complex image analysis is limited to a few classification algorithms and the ability to display Red, Green and Blue (RGB) representations of different bands. The ability to view images with different bands assigned to each of the three colors is very helpful, but insufficient for the problem of fully distinguishing rock types spectrally. For instance, you could look at vegetation cover in some detail with a standard 4|3|2 image, or ashes and tuffs with a 4|5|2 image. However, the images would not display other surface units in such a way as to be easily distinguishable.

The "4|3|2" and "4|5|2" designations are a convenient short-hand for labeling an image in which band 4 (near-infrared) brightness data is displayed as the red value for each pixel, band 3 or 5 (red or infrared) brightness is displayed as green, and band 2 (green) brightness is displayed as blue. Creating this sort of false-color image is the simplest, and thus quickest, type of image processing. For an example of its use, note how vegetation stands out as brilliantly red in a 4|3|2 image (Fig. 1). This is due to the

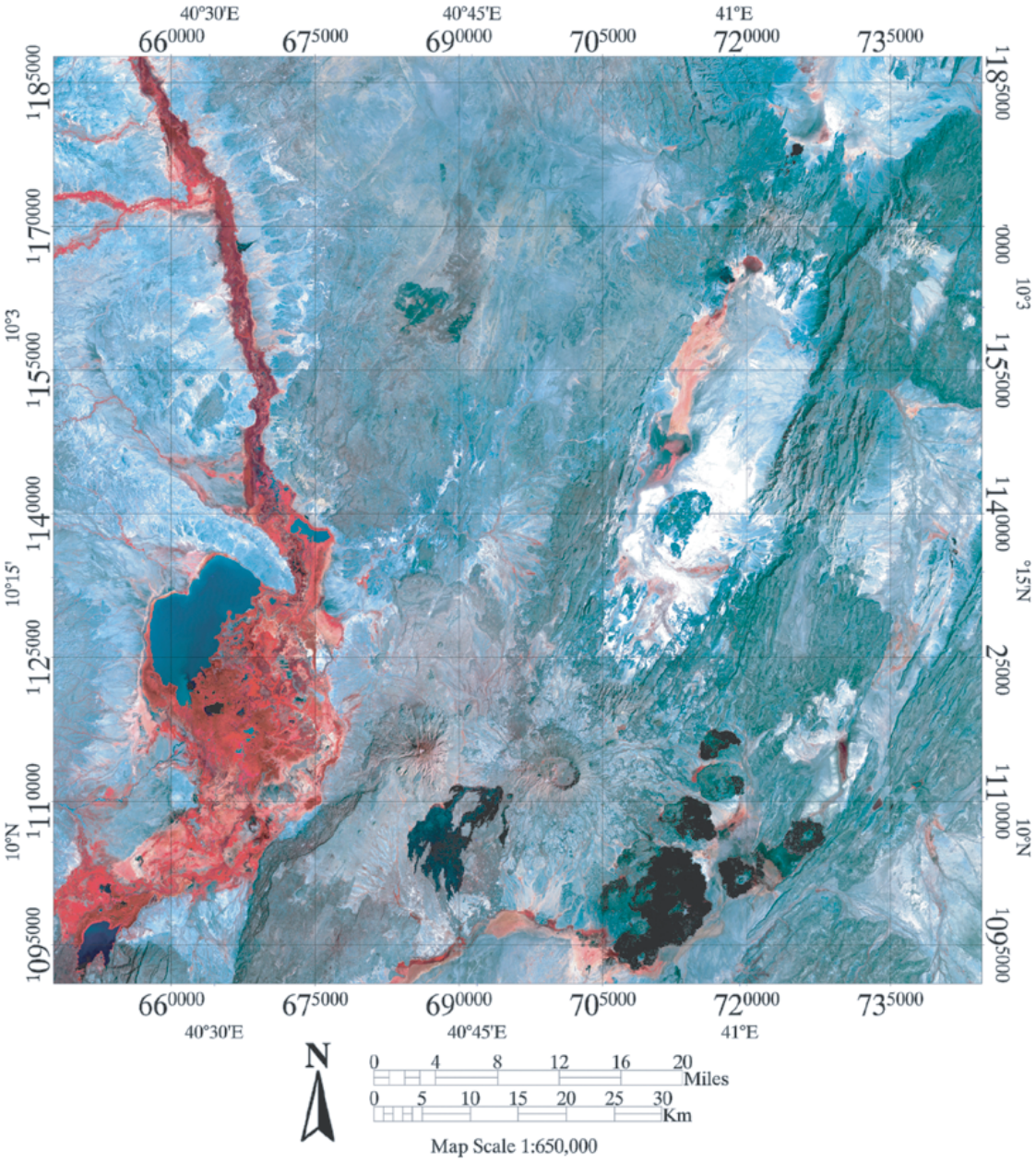

Fig. 1- Standard Landsat false color composite image (bands 4, 3, and 2 as RGB) of a 9,333 km^2 area in the Afar, along the Awash River. Most vegetation is concentrated along the river (running south-north in the west) and associated waterways.

high absorbance by chlorophyll in the visible wavelengths, combined with the high reflectance at VNIR (Very Near InfraRed) wavelengths by plant cell walls. This high reflectance at infrared wavelengths is thought to help prevent the breakdown of chlorophyll by heating (chlorophyll is unstable above 70ºC) (Drury, 2001). Figure 2 is an example of a 4|5|2 image, in which tuff and ash should stand out as bright green, due to their high reflectance in band 5 (true of most minerals, actually) and the absorption in band 4 by iron oxides (Jutz and Chorowicz, 1993).

Looking at the varying relative brightness's of different substances in different wavelengths and exploiting them to create an image in which they can be somewhat quantitatively grouped into different classes is the foundation of any mapping performed from satellite imagery. However, MultiSpec is far too limited for anything more complex than false-color images. Research System's ENVI 3.5 image analysis program provides a much greater array of options for enhancement, classification, and mapping. Although many of its features are oriented to analyzing hyperspectral and radar remote sensingdata, which are unfortunately unavailable at this time for the Afar, some of those can be of some use with broad-band spectral data, and it also has many basic image manipulation tools of use with any sort of data. Most of the following image manipulations were developed over the past few decades by different investigators, but are implemented in a convenient graphical interface in ENVI.

Basic Enhancement

Raw data, as downloaded from GLCF requires processing for analysis. Unenhanced spectral information on the earth's surface is usually very low in contrast.

Fig. 2- 4l5l2 false-color composite image. Ash and tuff surfaces are stand out as green to bright-green. Note possible spatter structures in magnified box.

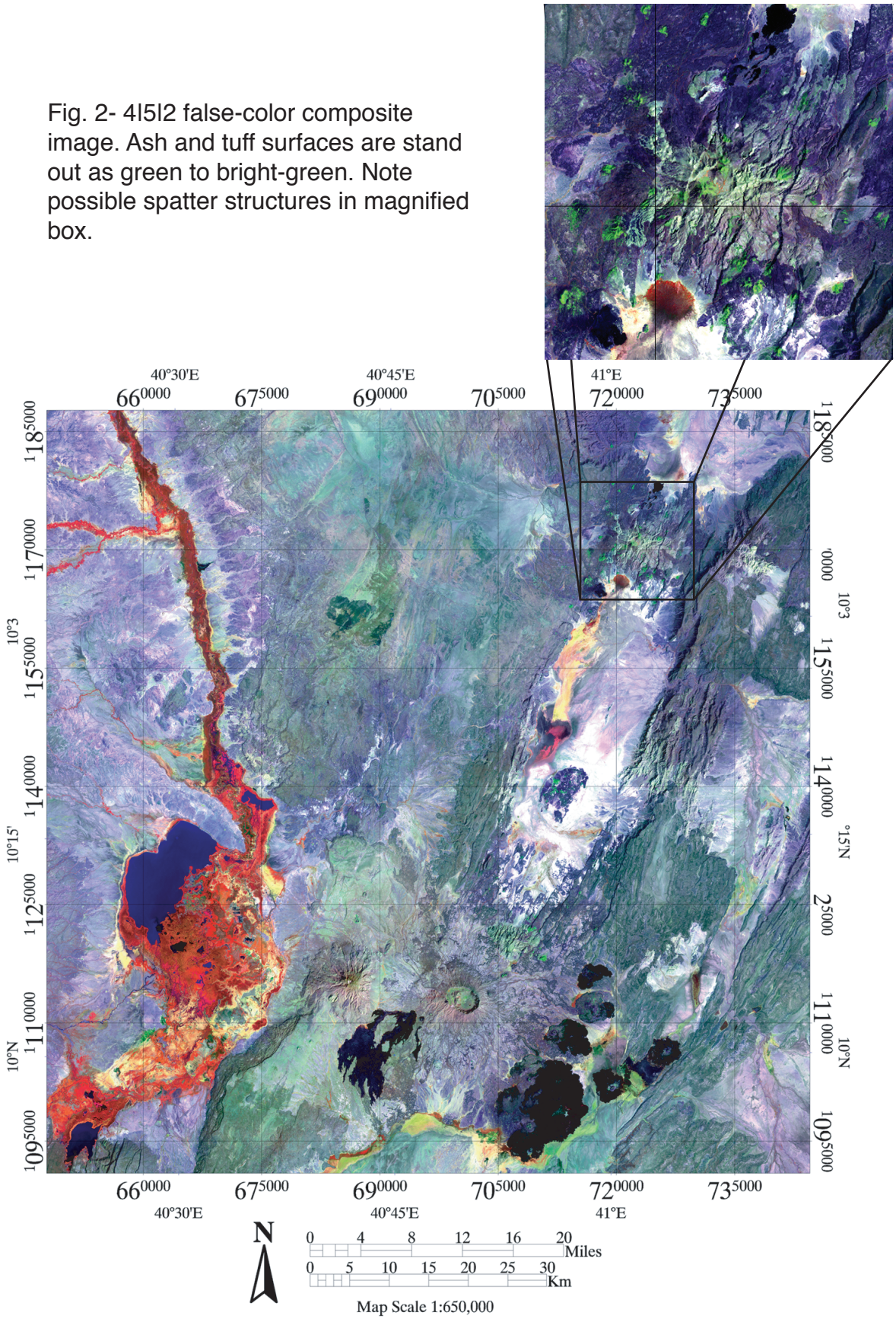

This causes an image to appear to be a sort of vaguely dark gray color, with some slight differences in brightness, often due to topographic shadows or albedo. Snow and clouds appear very bright, particularly in visible wavelengths, heavy shadows appear somewhat dark, and water always appears very dark, particularly in infrared wavelengths. Essentially, the base state of a picture of the earth's surface at a given wavelength is for most pixels to be tightly clustered around some brightness level ("digital number" or "DN" in image enhancement terms) between 0 (black) and 255 (white). Contrast can be enhanced by redistributing all the pixels in such a situation so that the ones in the highest DN bin are set to 255 and the lowest to 0, with all other bins distributed equally in between, preserving their relative positions along the brightness scale. This is known as a linear stretch, and is nearly always the first enhancement step for interpreting images.

A related basic enhancement is that of atmospheric subtraction. Some images can appear hazy due to atmospheric scattering and clouds, particularly at visible wavelengths. Rayleigh scattering of light at visible wavelengths is most intense for short-wavelength light, resulting in our blue sky on clear days, and without it, shadows would be perfectly dark in situations with only one light source. Scattering is much less intense at lower wavelengths, and is nearly nonexistent in the infrared. This means that the difference in brightness in shaded areas of an image at infrared (ETM+ band 7, for instance) and that same image at visible wavelengths is approximately equal to scattering intensity (Drury, 2001). However, actually subtracting this value from data results in extremely dark shadows, which can bias spectral analysis. Given that spectral analysis is mostly what I am trying to apply in this project, scattering subtraction was not worth the possible gains, and I ended up discarding the test scattering-corrected images I created.

PC Decorrelation Stretching

A more conceptually complex image enhancement, which was much more useful in spectral mapping, is principal component decorrelation stretching. As noted earlier, each band image tends to be fairly self-similar, and needs to be contrast-stretched for any spatial detail to be visible. Unfortunately, this is also the case between bands. In relatively broadband spectral resolution data, many dissimilar materials have essentially the same low-resolution spectral signature, and homogenous pixels are rare in any case (Fig. 3). PC analysis essentially takes a set of data (which might be represented as a bivariate scatter plot for 2 bands, a trivariate plot for three, etc.) and refits it to a new coordinate system. The new axis originates at the mean of all the data, with axis extending in the directions of greatest variance.

The PC transformed data, which has been fitted to an axis along the statistically determined directions of greatest variance (the successive Eigenvectors), can now be linearly stretched to further inflate the data in those directions, which results in a hugely better contrast gain than would be arrived at with a linear transformation along the original axis (Fig. 4). Using the inverse of the original Eigenvector to transform the stretched data back into the original band space returns it to its original color, while preserving the PC stretched increase in contrast (Kenea, 1997). This technique can be applied to any color image (i.e. one which contains information from more than one band of data) to enhance otherwise very subtle color variations, and thus is often a secondary step to another image enhancement, to maximize the visible differences one is trying to create between geologic units or any other kind of surface.

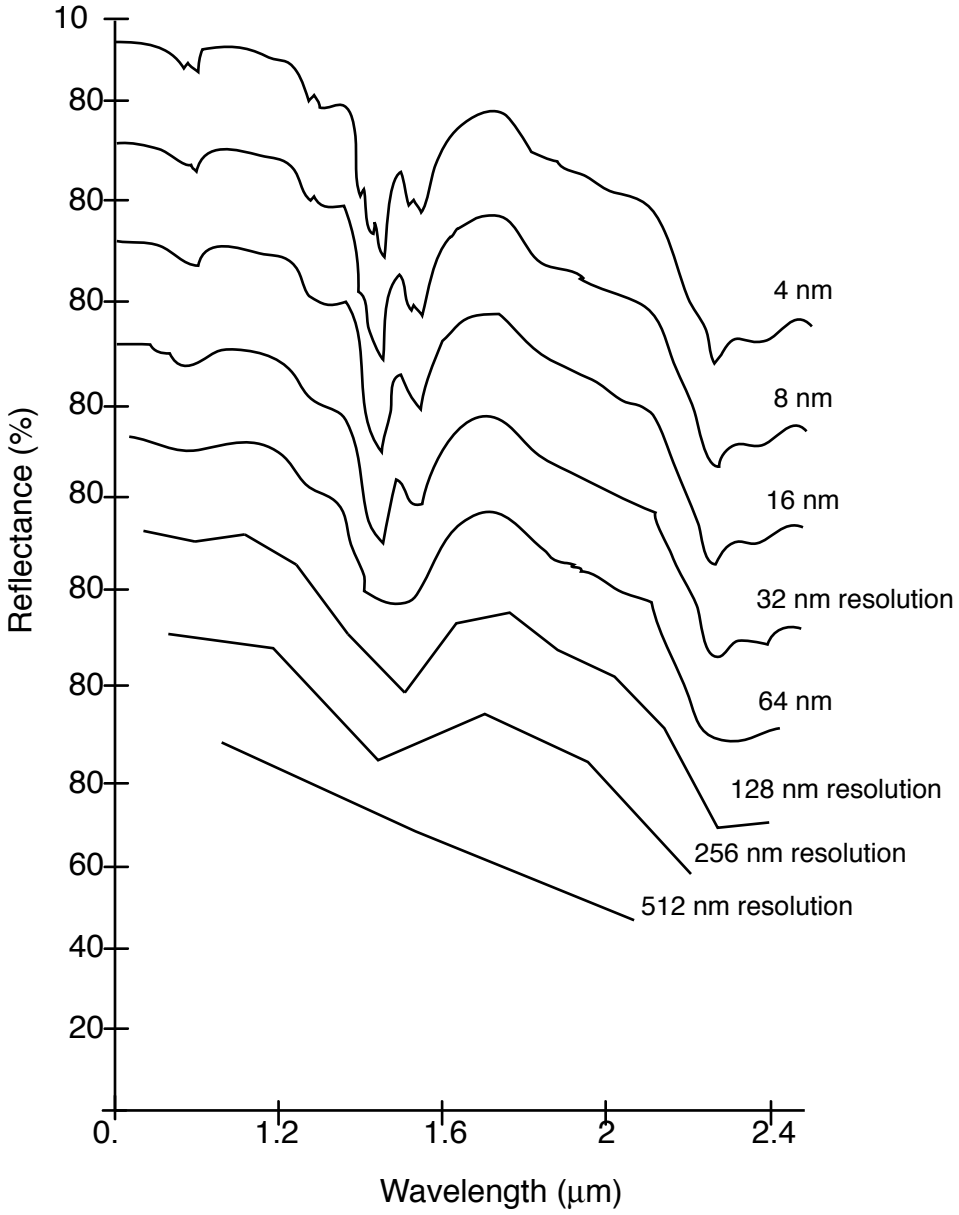

Fig. 3- Reflectance spectrum of gibbsite at a series of spectral resolutions (adapted from Cloutis, 1996). Note that Landsat 7 resolution ranges from ~60-70nm for visible bands to ~140-270nm for infrared bands, and that infrared bands are those in which mineral spectra are most variable.

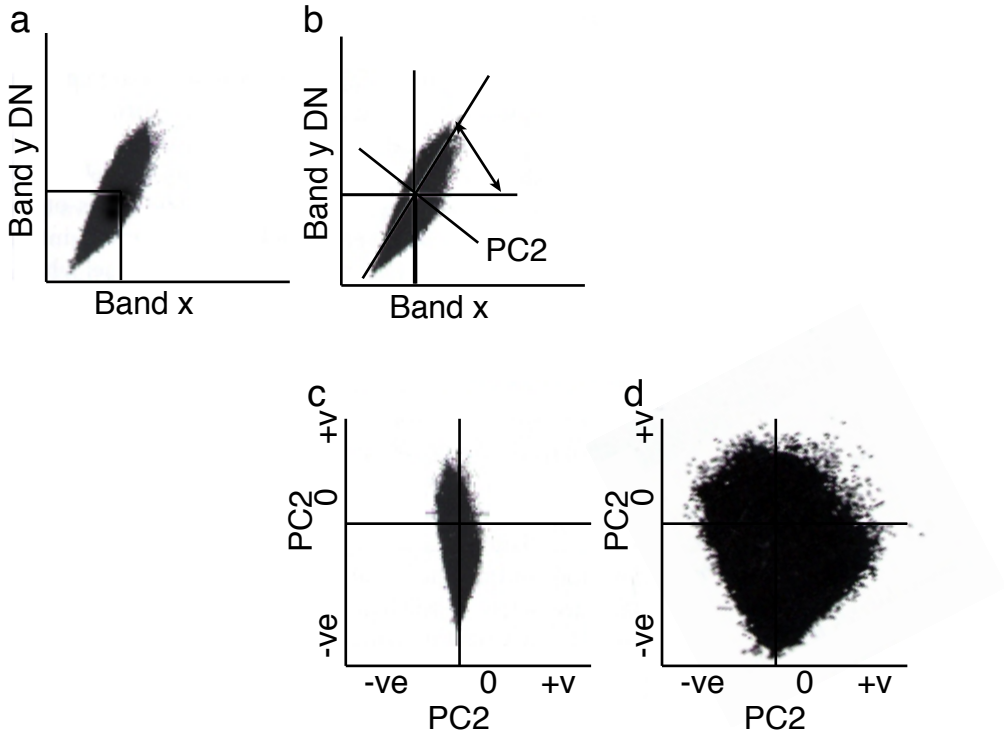

Fig. 4- Principal Component transformation for hypothetical bands x and y. Most combinations of bands from a Landsat scene will produce a highly correlated ellipse of points when graphed as a bivariate plot (a). Finding the lines of maximum stretch in two different dimensions (b) and defining those lines as the new axis (c) maximizes the decorellation possible with linear (axis-parallel) redistributions of data (d) that preserve color information (adapted from Drury, 2001).

Another result of PC transformation is that the data can be revisualized as a set of images that each represent a diminishing proportion of the variance in the data. The first image (PC 1) represents data values for the first PC axis, which was defined as the direction of greatest variance, and thus it tends to represent the vast majority of the contrast and thus spatial information in a data set, essentially consolidating all the contrast information from the six bands of ETM+ spectral data into one image. Each successive PC image contains less and less spatial contrast and more of the random noise (Gillespie et al., 1986).

However, each successive image also contain unpredictably variant loadings of information from the different spectral bands used to create them, and so a table of the Eigenvectors quantifying this loading must be used in analyzing PC images. In fact, a PC image with a highly positive Eigenvector for band *a* and a highly negative Eigenvector for band *b* and near-zero Eigenvectors for all the other bands is essentially the same as an *a*/*b* ratio image (Drury, 2001). However, band ratios are a much simpler and computationally quick way to arrive at the same result, albeit without the increase in spatial clarity. Fortunately, Landsat 7 was upgraded from its predecessors to include a method for increasing spatial resolution in a way easily integrated with its spectral data that I will discuss later.

Ratio Images

Band ratioing is the image enhancement technique that proved to be by far the most useful for spectral mapping in the Awash area of the Afar. Essentially, this is a technique for combining the information from two different bands, wherein the

brightness (DN) for a given pixel in one band is divided by the DN of its equivalent pixel in another band. The resulting image thus represents the "ratio" of brightness information for the two bands. This technique has a number of useful attributes, all of which are applicable to the Awash.

First, band ratioing can help eliminate the effect of varying illumination. Shadows caused by cliffs, gulleys, mountains, and other topographic features cause differences in brightness that are easy to misinterpret as lithologic boundaries when one is attempting to assess a large area, whether visually or with a computer algorithm. A single band image displays absolute brightness for a given surface, which is different for that surface depending on whether it is in shaded and fully lit conditions, which are often adjacent. Ratioing, however, can help eliminate shadows, as the given surface should have the same reflectance properties in both shaded and fully lit conditions. That is, when some lit pixels of a surface are divided by analogous lit pixels at another wavelength, and some shaded pixels of an identical surface are divided by their respective analogues at the other wavelength, the results should be the same (Vincent, 1997).

Second, the ratio of two bands can actually enhance the expression of otherwise indistinguishable changes in surface reflectance. Whereas in single-band images, the appearance of two adjacent surface units may be very similar, their differences become accentuated when two bands are ratioed together. Adding the information from more bands improves the potential for surface discrimination in an image, in much the same way as adding more and narrower bands would improve the overall ETM+ data set's spectral resolution and therefore its surface discrimination potential. This is why ratioing

was utilized in creating images for rock unit mapping. There is a lot more information in, for instance, a 1/2|7/5|3/1 (R|G|B) image than a simple 4|3|2 image.

Third, spectral ratios from satellite images can be more directly related to laboratory reflectance spectra of rocks and other surfaces, due to the "ironing out" effect mentioned above. A single laboratory spectrum can't possibly take into account the varying brightness of a material when seen in the field from orbit. However, ratioing can largely eliminate those effects, and in practice, the major limiting factor for matching lab spectra ratios to satellite spectra ratios is that pixels (the most specific unit of information in a given image) tend to be inhomogeneous, and thus difficult to match with very specific spectra of very homogenous lab materials (Drury, 2001). This was a major limitation of the mapping project.

IHS Datamerging

As noted earlier, Landsat 7's most notable upgrade from its earlier incarnations is its improved spatial resolution. In addition to the six bands of spectral data at 30m/pixel resolution, the ETM+ instrument has a panchromatic 15m/pixel band (band 8) with excellent spatial resolution. However, again the problem arises of combining information from separate bands into a useful image that incorporates as much information as possible. One problem with combining this band 8 high-resolution data with that from other bands is that the images are at different scales. All the Landsat bands are processed into quadrangles of equal land area and position, which is obviously helpful for organization, but higher resolution data equates to more pixels, and thus data that is matched with its low resolution counterparts geographically, but not pixel for pixel. Some

form of processing needs to be undertaken to combine all Landsat data into one image combining the advantages inherent in each band.

ENVI actually includes two so-called “Image Sharpening” algorithms for working high resolution topographical data into hue-dependant spectral-oriented images, and at least one other involving principal components has been used in other studies (Yesou et al., 1994). The most useful of the three is labeled in ENVI as “HSV Sharpening” (Hue, Saturation, Value, Sharpening), but is better known in the remote sensing literature as IHS (Intensity, Hue, Saturation) datamerging. This technique first takes any normal image that has been represented in RGB space and transforms it into IHS space. This means that data originally represented as three sets of pure brightness values and given arbitrary hue for display as red, green, and blue on a computer screen are reinterpreted as three entirely new data files.

These new data categories are best thought of in terms of a standard color wheel. Hue is akin to the angle on the wheel (i.e. what color), saturation represents where along the line from the centre of the wheel (completely pastel, all grey) to the outside edge (pure colors, with no grey) along the hue angle a pixel lies, and intensity defines the brightness of that pixel. Hue and saturation data will be somewhat abstract, and can’t really be imaged as single data files, but intensity is going to look just like one of the original black-and-white files from the RGB image we started with, except that it is a summary of their resultant RGB brightness. Thus, we might replace the intensity component of our IHS file and still retain its hue and saturation, which contains all the color information from the RGB original, and thus all its spectral information (Jutz and Chorowicz, 1993). At this stage, the ETM+ band 8 information is introduced as the new

intensity file, and the hue and saturation files simply need to be linearly stretched to the new pixel dimensions to create a complete new IHS image, which can be converted back into RGB space and displayed or manipulated normally. The new RGB image now contains all the color data of the original, with all the vastly improved spatial resolution of ETM+ band 8. This sharpening was possible before Landsat 7 came into service, but it involved combining information from multiple image sources (often in incompatible data formats), and therefore large potential sources of error in registering slightly different images of the same geographic location from different sources.

Classification Methods

Creating a PC-decorrelated ratio image sharpened with an IHS transform high-resolution intensity replacement may help to maximize the information visible in a given Landsat 7 scene, but this process of image enhancement is only the first step in geologic mapping. The necessary next step is interpretation, and deciding which colors represent which rock or vegetation units is by far the most difficult part of mapping with satellite data. Landsat scenes are cover quite large land areas, and terrains are often extremely diverse in appearance, with confusing patterns of vegetation cover and human development mixed with waterways and lakes, rock outcrops, and exposed sediments. However, there are computer functions that can help simplify the process of identification. Supervised classification requires user input for the demarcation surface units. The other types of functions are methods of unsupervised classification, in which the computer does more of the work.

Supervised Classification

There are many supervised classification algorithms in ENVI, but all require that the user define polygonal chunks of regions as different classes, and then calculate which pixels in the rest of the scene are similar enough (by user-defined limits) to be added to your classes. The method by which the computer works out this problem can be as simple asking the user for the dimensions of a box to put around the pixels of each user-defined class in three dimensional color space, and then grouping all pixels, already classed or not, that fall inside those values. It can also be very complicated, the most complex option being "Neural Net" classification, which takes an extremely long period of time to process for little apparent gain in accuracy, and involves a layered feed-forward neural network, using standard backpropagation for supervised learning (RSI, 2001).

The purpose of all supervised classification methods are the same, but the varied results of supervised classification can be very frustrating when working with areas the size of an entire Landsat scene. There is so much variation that it can be difficult to define enough properly differentiated classes to include all the important variations in the scene. Some significant lithologic boundaries exist that can be difficult to define to the degree that the computer can differentiate between them, even with the most extensive and thoughtful image enhancement. In smaller images, these techniques are much more effective, as it is generally easier to see how many classes it should take to define all elements in a small area. Thus, while I experimented with supervised classification extensively, it was not an efficient way to classify full Landsat scenes worth of data.

Unsupervised Classification

Unsupervised classification, wherein the computer decides how to define classes, seems to provide much more consistent and comprehensive results for large scenes, which is what this project focuses on. For the two different unsupervised algorithms that can run under ENVI, user input consists not of defining classes, but of defining how variable a class is allowed to be as the computer creates it, the number of classes desired, and other parameters that essentially define how long the computer is allowed to think about the problem. This is a very important parameter, as the ISODATA and Kmeans algorithms can take fairly high-end PC's many hours to run on full Landsat RGB composite scenes. Both algorithms work by plotting all pixels into n-dimensional space (where n is simply the number of band inputs) and finding clusters of pixels with vectors to their cluster's center not exceeding the maximum user-defined variance (Vincent, 1997). Given enough time to run, both algorithms seemed to yield essentially the same results (Fig. 5), but I found that in a purely qualitative way, ISODATA classification tends to look more accurately correlated to patterns visible in the image being classified.

Radar Remote Sensing

Visible and near infrared are not the only parts of the electromagnetic spectrum being used to investigate landforms from orbit. Radar and thermal wavelengths can provide extremely valuable information. Some advantages of long wave radiation include its tendency not to interact with the atmosphere, radar reflectance's correlation with surface texture as well as crystalline or chemical structure, and its potential to be generated easily as coherent waves by sensing platforms. These properties make possible

a.

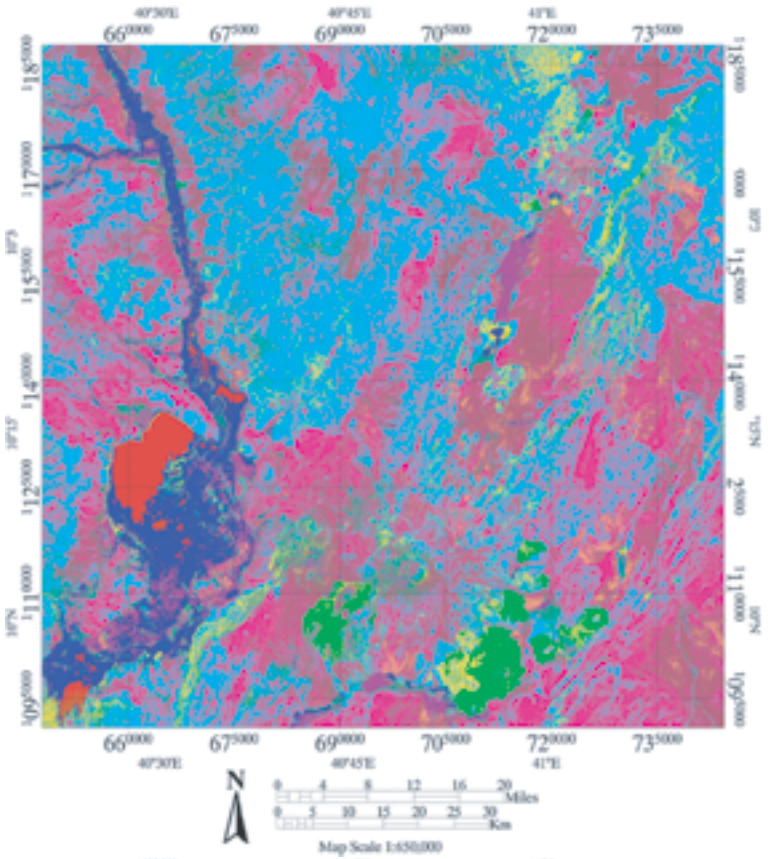

b.

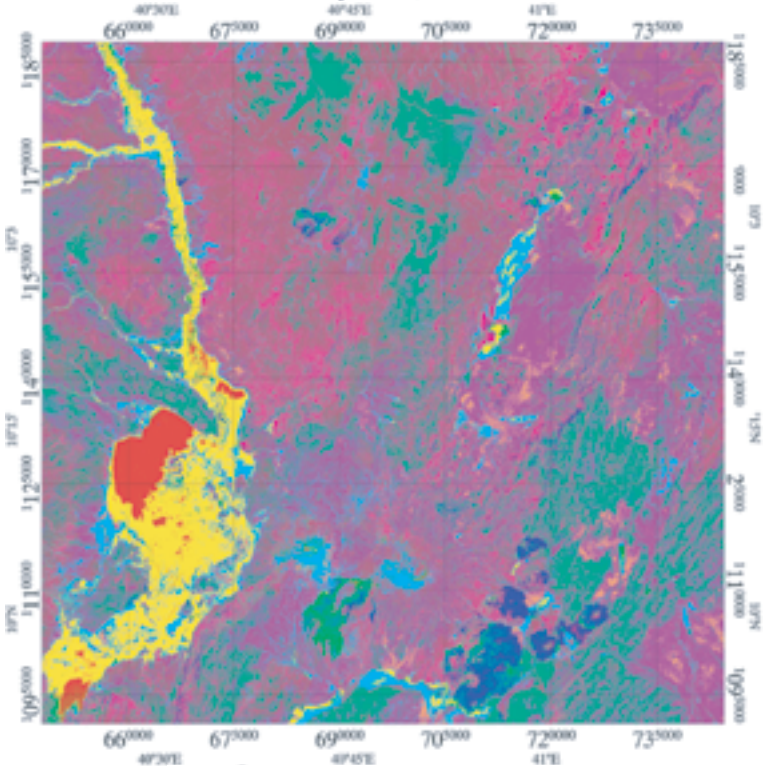

Fig. 5- Results of ISODATA (a) and Kmeans (b) classifications.

active remote sensing from orbit, which implies that it can work in all weather and lighting conditions (Drury, 2001).

Radar reflectance does depend on surface chemical composition to some degree- the dielectric constant of a material (very high for water and metals, low for dry soils and some rocks) determines how much radar energy will penetrate its surface, in radar-smooth conditions. However, in practical field conditions, most surfaces are too rough for radar penetration, as radar reflectance is much more sensitive to the texture of a surface than its composition. Smooth surfaces reflect very little energy straight back at the emitter and will appear dark in a radar image, while rough surfaces are like a collection of small corner reflectors, and will appear bright (Dong and Leblon, 2004). Some investigators have attempted to develop methods for analyzing texture information and correlating it to specific materials, but such analysis is outside of the scope of this project.

Elevation Modeling

This project investigated radar information for its elevation measurement capability, and thus topographic mapping potential. When two receivers of known separation are receiving the same radar reflection, the differences in the signal the two receivers record can be employed to derive a distance to the reflecting surface. This is known as interferometry, and was employed by the Shuttle Radar Tomography Mission (SRTM) to map about 80% of Earth's surface, over the course of about 222 hours of data gathering; this eleven-day mission in February 2000 generated about 12.3 terabytes of three-dimensional data, which is actually still being processed to USGS map standards (Ramirez, 2005). However, the GLCF has made preliminary SRTM elevation data

available in a few different formats. It still contains some holes, particularly over bodies of water, but it is mostly complete. ENVI has a convenient function for filling holes by inferring elevations from neighboring good pixels, which at least eliminates drastic irregularities, although it tends to map lakes as equal in elevation to their shores, which is clearly incorrect, but for my purposes doesn't matter.

Elevation data was primarily utilized to help visualize the terrain being imaged. It can be very difficult to get any sense of varying elevation or relative sizes from a straight-down view. Ridges can look remarkably similar to valleys, especially when they appear to be made out of the same materials, and none of the colors equate to what you would see with your eyes. Fortunately, ENVI can interpret SRTM images (Fig. 6) as digital elevation models, and revisualize them in a few very useful ways. First, it can create an artificial hill shade image, for which one can indicate the elevation and azimuth of the illumination source, and ENVI will calculate the resultant appearance of the topography. A relatively low elevation value results in an image with very sharply shadowed topography (Fig. 7), making it obvious where the ridges, mountains, valleys, and rivers are located.

The other useful topography visualization method in ENVI calculates a three-dimensional wire-frame model from digital elevation data, which can either be viewed as such, or with an image texture-mapped onto it (Fig. 8). This elevation visualization method is much more interesting than hill shade imaging, and makes it even easier to relate spectral characteristics of an image to topography. The ability of the ENVI graphics engine to allow live rotation and magnification of the texture-mapped model can

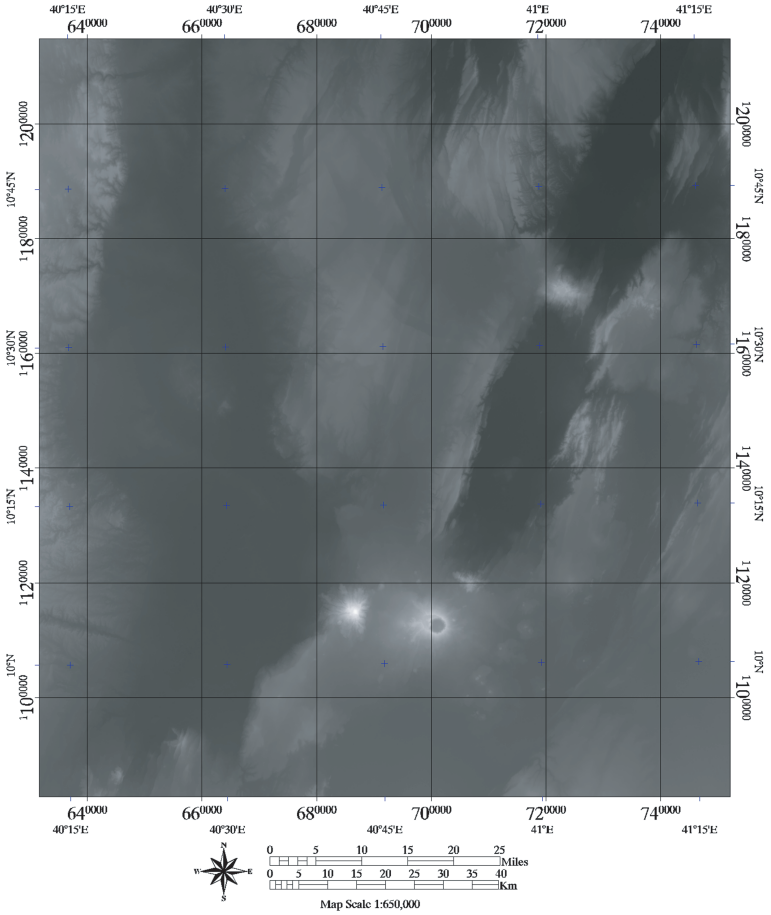

Fig. 6- Unenhanced SRTM image (from GLCF, 2004).

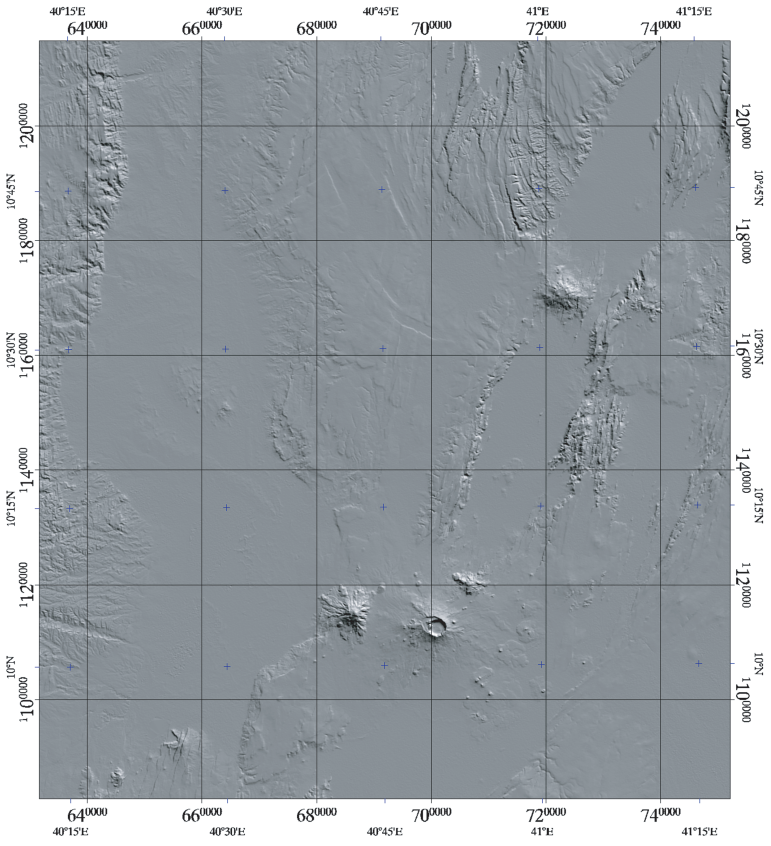

Fig. 7- Artificial shade image; illumination source azimuth 30º, elevation 30º.

Fig. 8- 4l3l2 composite image (see Fig. 1) texture mapped to SRTM three-dimensional elevation model.

be the most useful mode in which to interpret images. It is yet another layer of information that can be added to an image to aid in interpretation.

Results

Figures 9 through 20 are 1/450,000 scale maps generated from a 4/1|3/1|7/4 ratio image datamerged with band 8 14.5m resolution spatial data, corresponding to a total mapped area (discounting missing data along the edges, and overlaps between figures) of ~33,700km^2. Figure 21 is an ISODATA classified map for the overall scene, with intentionally general surface units interpreted as accurately as possible. The ISODATA classification image was calculated from a different image than is presented in Figures 9-20 so that the computer could differentiate between certain apparent basalt flows and water, both of which have the same (very low) reflectance in all bands except band 1. This includes the high-resolution band (8), which samples at 0.52-0.9μm wavelengths (a range equating to bands 2, 3, and 4 combined), so the brightness data added from the IHS datamerge tends to darken both basalts and water to the same black color, precluding discrimination. The results are still not completely accurate, but are the best that could be achieved for differentiating such similar surfaces.

Discussion

Map figures 9 through 12 depict the southernmost strip of terrain in the selected Landsat 7 scene. Figure 9 is located at the southernmost end of the Afar valley, where the Main Ethiopian Rift expands out from the Eastern Branch 40-80km wide horst and graben structure to the much wider triple junction area. It is dominated by rift valley floor

sediments. The city visible as a conglomerate of rectilinear features at 9º26'N, 40º13'E is Awash. There are clear structural features running Ethiopian Rift-parallel, roughly SSW-NNE, down the center of the figure. Although it is unclear in the figure, mapping the terrain as a texture on a three-dimensional DEM reveals these structures to be steeply WNW-dipping sections of otherwise gently sloped hillsides. They appear black due to shadowing effects. These cliffs lie in a section only lightly vegetated, and thus could very well be erosion related, possibly expressing rift-related faults or horst and graben structures in the basalts that likely underlie most of the valley.

Relatively pure blue colors in a 4/1|3/1|7/4 image often indicate rocks with high iron content by virtue of their high reflectance in band 7 and absorption in band 4. Thus, most of the unvegetated surface in the lower half of Figure 9 is likely to contain ash or tuff. The very bright white sediments at the foot of the reddish (likely vegetated) highlands just visible in the southeast corner of Figure 9 are probably white because their high albedo created saturated pixels in the bands being displayed, which could mean that they are covered in salt crusts that are precluding much vegetation growth.

Further north and to the center in Figure 9 lie a few very dark blotchy areas. The very elongate one running from 9º40' to 9º50' is almost certainly a well-exposed, relatively young basalt flow, and it seems likely from inspection in 3-D that it is surrounded by a very subtle ring of local topographic highs expressing ash or tuff spectral signatures roughly parallel to the river flow and hillside cliffs. I interpret this to possibly indicate a very old volcanic crater structure.

Just north of this basaltic area is the first in a string of lakes that are difficult to differentiate from the basalt flows in this image based on color. However, they tend to

have spatially distinct edge patterns, and be surrounded by a distinctive red ring of vegetation. To the northeast is the beginning of an older basalt flow that is apparently fairly thick, and now forms a local topographical high as a plateau structure.

Figure 10 depicts the area immediately east of Figure 9. The southern half of this area is characterized by a transition from foothills in the southwestern area to the highlands in the southeastern area, which tend to have more rugged shapes, and are mostly covered in vegetation. However, the telltale blues and bluish-purples of volcanogenic terrain with high iron content are still visible, particularly on the series of small (~1km in width) purple cones scattered across the large hill trending west to east, leading up to the large (1876m) mountain. For geographic reference, this mountain is ~20km north of Asbe Teferi; the Asbe Teferi-Harer roadway is just visible to its southeast. Based on its spectral characteristics, it seems that the vegetative pattern of this mountain is the reverse of that found at northern latitudes- vegetation density seems to increase towards its peak, from the ash cone-like spectral signature near its base.

The terrain directly to the west (across the river) and northeast of the mountain appear to be very weathered and somewhat weathered basalt surfaces, respectively, although the western terrain appears to be too weathered for easy identification. Further east, there is apparently a vegetated drainage of some sort, then the beginnings of the rift valley's southeastern border highlands, which are essentially enormous horst structures. This terrain is extremely rough in appearance, and appears to get higher rainfall than the valley floor, based on the near-total vegetative cover.

The northern half of Figure 10 is characterized by more apparently salt-impregnated sediments in the lowlands, intermixed with the darker blue volcanogenic

sediments. In the highlands to the northeast of the figure, the blue spectral signature of the local volcanics is combined with the smooth and highly reflective spatial signature of an older basalt surface for easy identification. Basalts in this area all seem to take on these round-edged, smoothed-out appearances at a certain age. Just visible at the northern margin of this figure is the very dark signature of another young basalt flow.

Figure 11 is clearly dominated by two terrains- the highly vegetated highlands to the south, and the valley sediments to the north, which are framed to the east and west by somewhat old basaltic plateaus. These plateaus are likely only obvious by satellite, as they are somewhat subtle in topographic expression, and tens of kilometers in extent. To the far northeast of this figure is another of the many large (>5km in diameter) lava and ash cones dotting the rift valley landscape.

Figure 12 contains only minimally more information than Figure 11, covering only a few hundred more km^2. However, it is the easiest figure on which to see the lineament trend of the Somalian Plate side of the Afar Rift. The red fluvial channels run in a generally northern direction, but that is just because the valley to the north is so much lower than the southern highlands. The structural lineaments appear to run east-west, perpendicular to the water flow, which may create the annular appearance of the waterways. Some other features worth noting are the two overlapping volcanic cones to the east of the near-perfect cone that was also visible in Figure 11. It is clear from the differences in brightness of the two overlapping features that they are of very different ages. However, it is only in 3D view that older structure can be identified. It turns out that the eastern part of the structure is much lower in elevation and smoothed, and thus older.

Just southeast of these small mountains is a basaltic plateau, which appears from its beautifully smooth surface to be quite old.

Figures 13 through 16 map a strip of terrain north of that mapped in Figures 9 through 12, through the approximate center of the Landsat 7 scene. The easternmost, Figure 13, takes us back to the Awash River. The vegetation surrounding this waterway, and the associated large lake (~16km major axis) tend to dominate initial evaluation of this figure. More interesting, however, is the oddly shaped drainage to the far southeast of this figure, which is probably the result of fairly recent uplift and rapid, ongoing erosion. Just out of the scene to the immediate east at this point is the edge of the western highlands. This geomorphic/tectonic feature, along with the petrological clue of huge amounts of volcanic fluvial sediment being deposited as the dark blue fan-shaped features at the outwash of the streams coming out of western highlands, may be evidence of recent or ongoing volcanic activity and uplift to the west. There is certainly evidence of recent (limited) uplift in the southeast of this figure- this nicely conic dead volcano is the highest point in the entire Landsat scene, excluding the far southeastern highlands.

Another prominent feature of this figure is the transition from river valley sediments (light blue) to the more rocky exposed basalt terrain in the east. Note that most non-fluvial linear elements in this figure are still trending in the same NNW direction, reflecting the general lineament trend along the Nubian Plate. However, as we will see, this is not the case for the entire scene.

Figure 14 contains the majority of the youngest looking volcanic features in the scene, concentrated to its southeast. The two ~8km diameter mountains each contain clear calderas (the eastern is much larger, of course), which appear to contain sediments

and older basalts. However, between the two (apparently dormant) volcanoes, and in patches to their east, are apparent basalt flows of very low albedo, implying rough, and thus likely quite young, surfaces. To the northeast of the eastern volcano is a dark blue area, which is a small topographic high, which appears to be a scattering of newer ash cones over another structure, old enough to be lineamented.

In the north of Figure 14 is long, narrow (~14km wide) valley, bounded to the south, east, and west by NNE lineamented basalt terrains. It is mostly covered in high-albedo sediments, presumably erosional products of the valley boundaries. There is a swath of anomalous yellow terrain, which melds into a black and orange feature at its southern termination. By definition, a yellow feature in 4/1|3/1|7/4 RGB space is a mixed pixel, which must be high in reflectance in bands 4 and 3, and low in reflectance in band 7. It seems likely that this is the drainage for the valley, wherein a swath of light vegetation leads down to a shallow lake, the southern end of which is very murky, and thus much more reflective in infrared than the apparently black clear water of the northern end. The similar black, yellow, and orange south-curving feature in the southwest of Figure 15 appears easily characterized as another shallow lake, especially considering the narrow red traces of streams feeding into it from the southern highlands. The beginnings of an extremely high-albedo terrain begins to the east, mostly in the southern half of the figure, which seems likely to be composed of salt encrusted soils or sediments of some kind, possibly evaporites. To the northeast, the terrain appears relatively old, and is strongly NNE lineamented.

Figure 16 is dominated by the extremely high-albedo terrain described in Figure 15. Little detail is visible for this area, due to the high number of fully saturated pixels.

The bright green feature to the northwest appears to be a lake, with small (1.5km in diameter) fans of sediment perhaps contributing to an unusually high iron content, which could produce its distinct spectral signature.

Figures 17, 18, 19, and 20 map the final northern strip of terrain in the scene, once again east to west. However, the overlap with the previous four figures is large. Again, the Awash River is the most prominent feature in the easternmost figure. The boundary between western river valley sediments and eastern mafic terrains occurs in Figure 17, just as in Figures 13 and 9. Note the clear trace of the road at around 10º45'N, 40º41'E. The anomalous yellow swath of fluvial sediment analyzed for Figure 14 is once again prominent in Figure 18. Similar features occur in the north of this figure, flowing down what appears to have once been part of the valley in Figure 14, before the volcano at 10º35'N, 41º02'E appeared. This uplift no doubt explains the seeming profusion of sediments in these two valleys.

Figure 19 seems to contain the junction of two lineament systems. The NNW trending structures clearly dominate its western half, but the terrains in the southeast seem to be lineamented ESE-WNW. Additionally, another lake in a large basin, murky with sediments, lies to the northeast of this figure. There does not seem to be any vegetation associated with this body of water, which seems unusual.

Figure 20 provides a more complete view of this unusual body of water. In this figure, the drainage of this lake to the north can be observed, where it seems to have created an alluvial fan of some sort, visible at the far north edge of the figure. Just east of that drainage is an interesting symmetrical valley, which may be a horst and graben structure.

Conclusion

This study confirms the utility Landsat 7 ETM+ data sets for synoptic mapping of surface units in a mostly arid environment like the Afar Rift Valley. Although compositional analysis cannot be certain without either better spectral resolution than Landsat 7 can provide or field data, this study's images of general terrains and structures, with units interpreted as far as possible, could be extremely useful in the field. Although figures were created here with large-scale feature interpretation in mind, maps at scales of 1/25,000 or better are possible while retaining good high resolution. Further mapping studies in this area could easily create much higher resolution maps, map lineaments quantitatively, and obtain more spectrally precise data for compositional analysis.

Acknowledgements

I would like to thank Bereket Haileab for making me work, reading drafts, and providing unique and exceptional information on the Afar. Cameron Davidson made this project possible by introducing me to the Carleton Geology Department's surprisingly extensive array of image analysis software. Many thanks to Kate Stalker for reading a draft, and Nick Swanson-Hysell for constructive discussion and Illustrator technical support. I am also, last but not least, indebted to the anonymous RSI employee who wrote the help file for ENVI.

References Cited

Abrams, M., and Hook, S. J., 1995, Simulated Aster Data for Geologic Studies: Ieee Transactions on Geoscience and Remote Sensing, v. 33, no. 3, p. 692-699.

Bowen, R., and Jux, U., 1987, Afro-Arabian geology: a kinematic view: New York, Chapman and Hall, 295 p.

Cloutis, E. A., 1996, Hyperspectral geological remote sensing: Evaluation of analytical techniques: International Journal of Remote Sensing, v. 17, no. 12, p. 2215-2242.

Dong, P., and Leblon, B., 2004, Rock unit discrimination on Landsat TM, SIR-C and Radarsat images using spectral and textural information: International Journal of Remote Sensing, v. 25, no. 18, p. 3745-3768.

Drury, S., 2001, Image Interpretation in Geology: Malden, Blackwell Science Inc., 290 p.

Getahun, Y. G.-E., 2003, Ethiopia in view of the NAPA Process, Climate Change and Air Pollution Studies Team, National Meteorological Services Agency of Ethiopia. http://www.unitar.org/ccp/Addis/presentation%206%20NAPA%20Ethiopia.pdf.

Gillespie, A. R., Kahle, A. B., and Walker, R. E., 1986, Color Enhancement of Highly Correlated Images .1. Decorrelation and Hsi Contrast Stretches: Remote Sensing of Environment, v. 20, no. 3, p. 209-235.

GLCF, 2005, Global Land Cover Facility. http://glcf.umiacs.umd.edu.

Jutz, S. L., and Chorowicz, J., 1993, Geological Mapping and Detection of Oblique Extensional Structures in the Kenyan Rift-Valley with a Spot Landsat-Tm Datamerge: International Journal of Remote Sensing, v. 14, no. 9, p. 1677-1688.

Kenea, N. H., 1997, Improved geological mapping using Landsat TM data, Southern Red Sea Hills, Sudan: PC and IHS decorrelation stretching: International Journal of Remote Sensing, v. 18, no. 6, p. 1233-1244.

Mengesha, A. B., 2000, Evolution of the Afar Depression from Orbital Optical and Radar Image [PhD proposal thesis]: University of Texas, 5 p.

Oppenheimer, C., and Francis, P., 1997, Remote sensing of heat, lava and fumarole emissions from Erta'Ale volcano, Ethiopia: International Journal of Remote Sensing, v. 18, no. 8, p. 1661-1692.

Pallister, J. W., 1968, International Tectonic Map of Africa: Institut Geographique National.

Ramasamy, S. M., Venkatasubramanian, V., and Anbazhagan, S., 1993, Reflectance Spectra of Minerals and Their Discrimination Using Thematic Mapper, Irs and Spot Multispectral Data: International Journal of Remote Sensing, v. 14, no. 16, p. 2935-2970.

Ramirez, E., 2005, Shuttle Radar Topography Mission, Jet Propulsion Laboratories. http://www2.jpl.nasa.gov/srtm/.

Renne, P. R., WoldeGabriel, G., Hart, W. K., Heiken, G., and White, T. D., 1999, Chronostratigraphy of the Miocene-Pliocene Sagantole Formation, Middle Awash Valley, Afar Rift, Ethiopia: Geological Society of America Bulletin, v. 111, p. 869-885.

RSI, 2001, The Environment for Visualizing Images: Boulder, Research Systems, Inc.

USGS, 2005, USGS EROS, Sioux Falls, SD. http://edc.usgs.gov/.

Vincent, R. K., 1997, Fundamentals of geological and environmental remote sensing: Upper Saddle River, Prentice-Hall Inc., 366 p.

Wiart, P. A. M., Oppenheimer, C., and Francis, P., 2000, Eruptive history of Dubbi volcano, northeast Afar (Eritrea), revealed by optical and SAR image interpretation: International Journal of Remote Sensing, v. 21, no. 5, p. 911-936.

Winter, J. D., 2001, An introduction to igneous and metamorphic petrology: Upper Saddle River, Prentice-Hall Inc., 697 p.

WoldeGabriel, G., Heiken, G., White, T. D., Asfaw, B., Hart, W. K., and Renne, P. R., 2000, Volcanism, tectonism, sedimentation, and the paleoanthropological record in the Ethiopian Rift System: Special Paper- Geological Society of America, v. 345, p. 83-99.

Yesou, H., Besnus, Y., and Rolet, J., 1993, Extraction of Spectral Information from Landsat-Tm Data and Merger with Spot Panchromatic Imagery - a Contribution to the Study of Geological Structures: Isprs Journal of Photogrammetry and Remote Sensing, v. 48, no. 5, p. 23-36.

-, 1994, Perception of a Geological Body Using Multiple Source Remotely-Sensed Data - Relative Influence of the Spectral Content and the Spatial-Resolution: International Journal of Remote Sensing, v. 15, no. 12, p. 2495-2510.

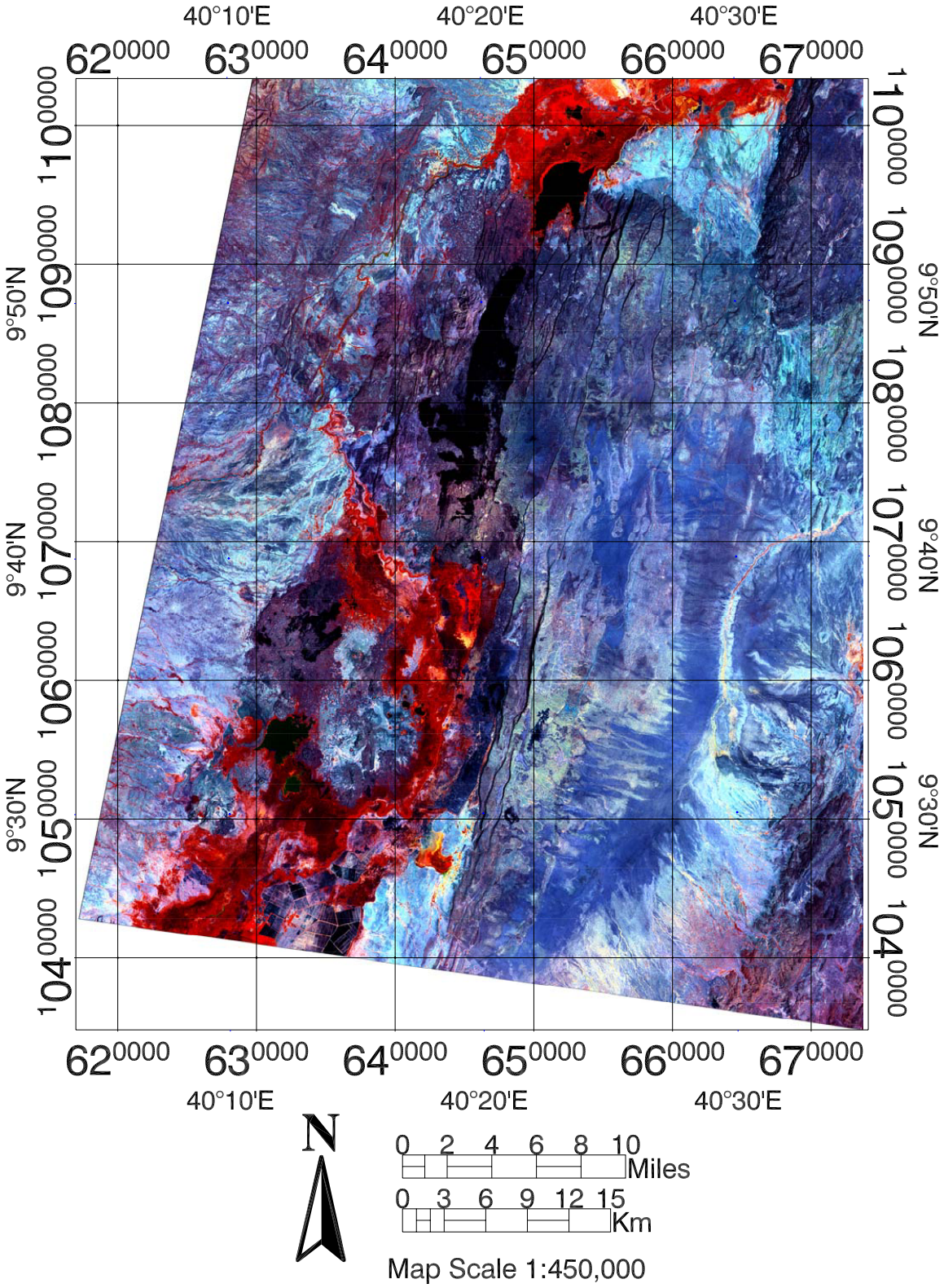
40°10'E
40°20'E
40°30'E
62 0000
63 0000
64 0000
65 0000
66 0000
67 0000
110 0000
109 0000
108 0000
107 0000
106 0000
105 0000
104 0000
9°50'N
9°40'N
9°30'N
N
0 2 4 6 8 10
Miles
0 3 6 9 12 15
Km
Map Scale 1:450,000

Figure 9

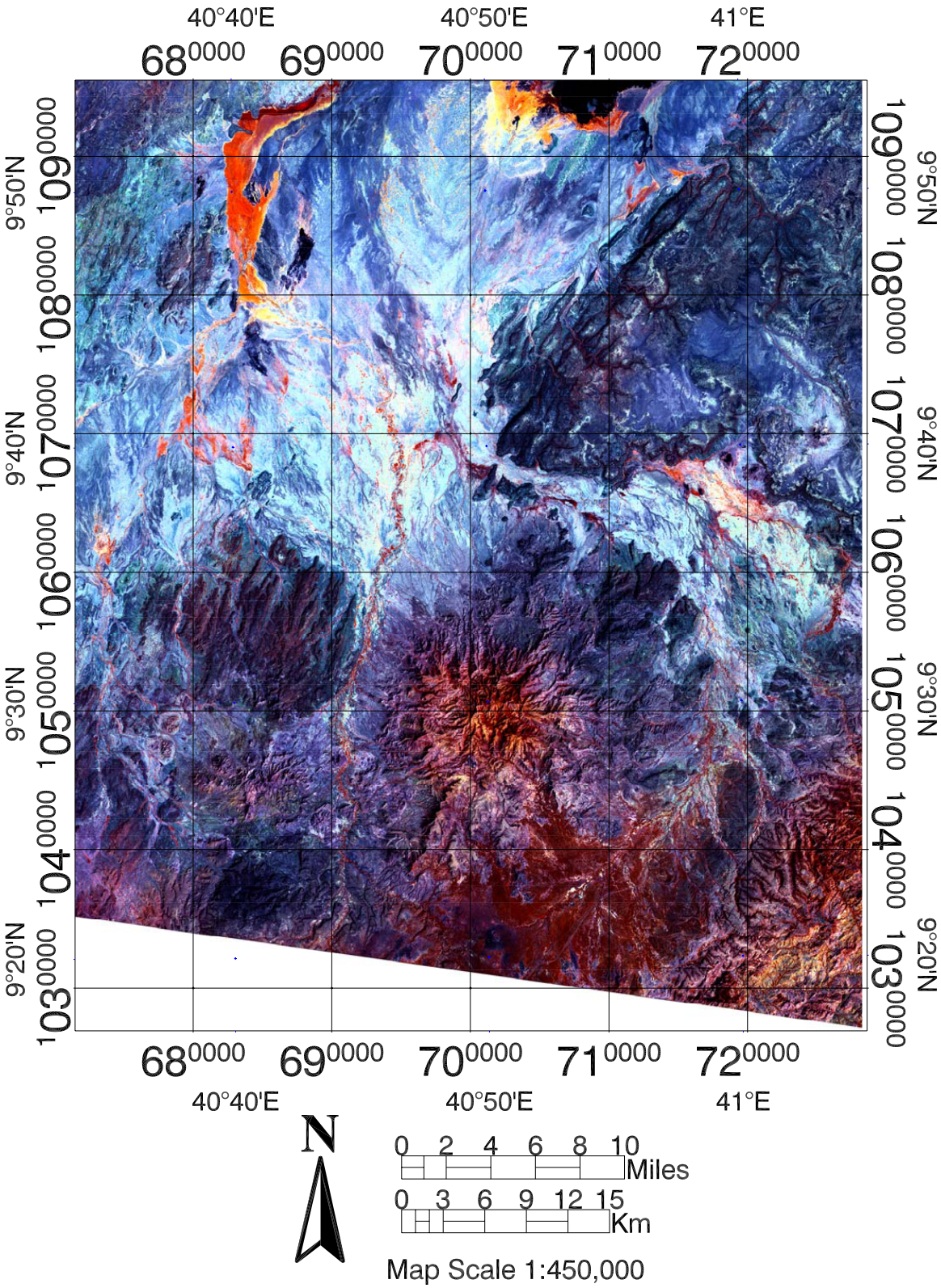
40°40'E
40°50'E
41°E
68 0000
69 0000
70 0000
71 0000
72 0000
9°50'N
9°40'N
9°30'N
9°20'N
109 0000
108 0000
107 0000
106 0000
105 0000
104 0000
103 0000
N
0 2 4 6 8 10
Miles
0 3 6 9 12 15
Km
Map Scale 1:450,000

Figure 10

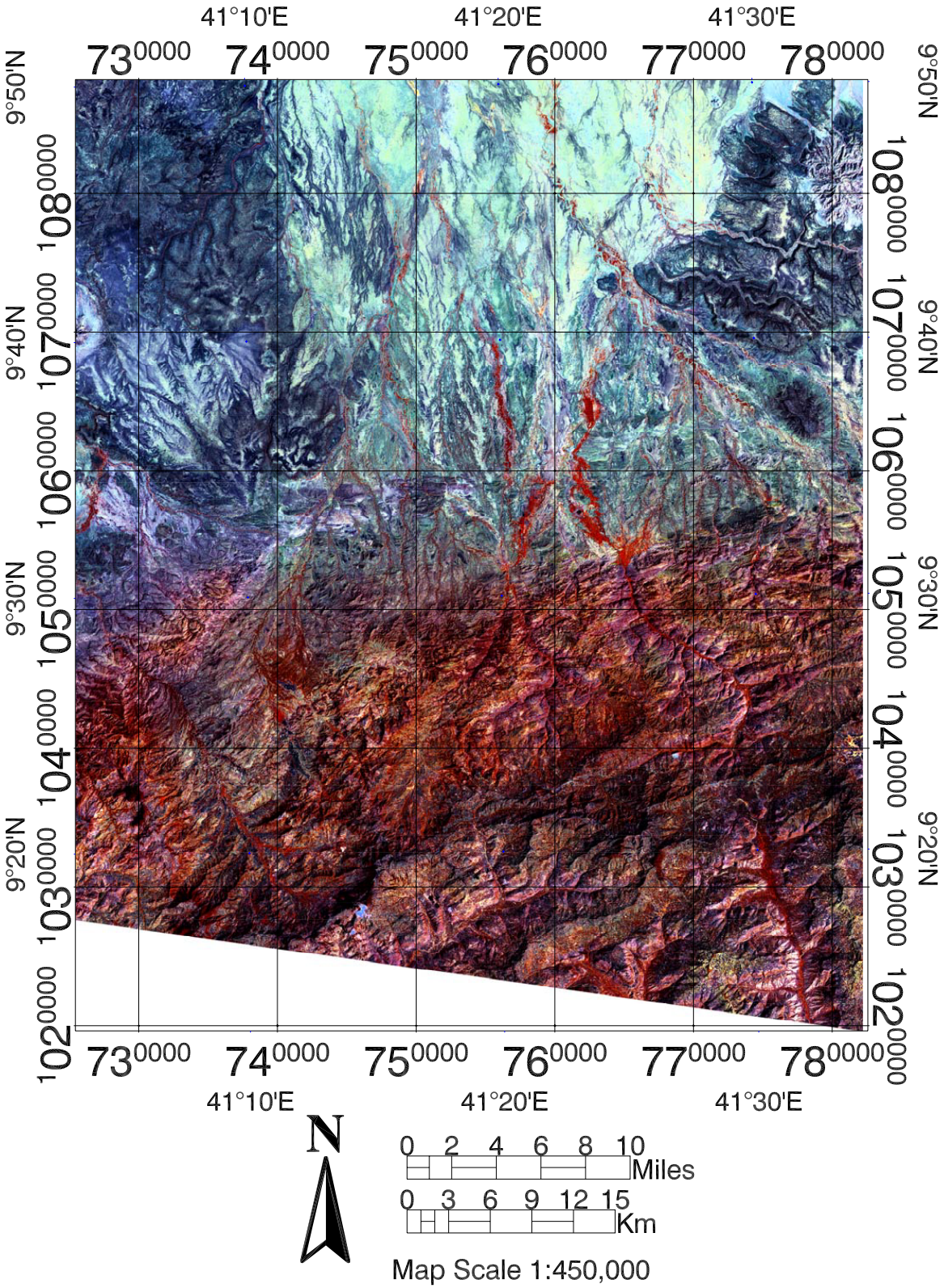
41°10'E
41°20'E
41°30'E
730000
740000
750000
760000
770000
780000
9°50'N
9°40'N
9°30'N
9°20'N
1080000
1070000
1060000
1050000
1040000
1030000
1020000
N
0 2 4 6 8 10
Miles
0 3 6 9 12 15
Km
Map Scale 1:450,000

Figure 11

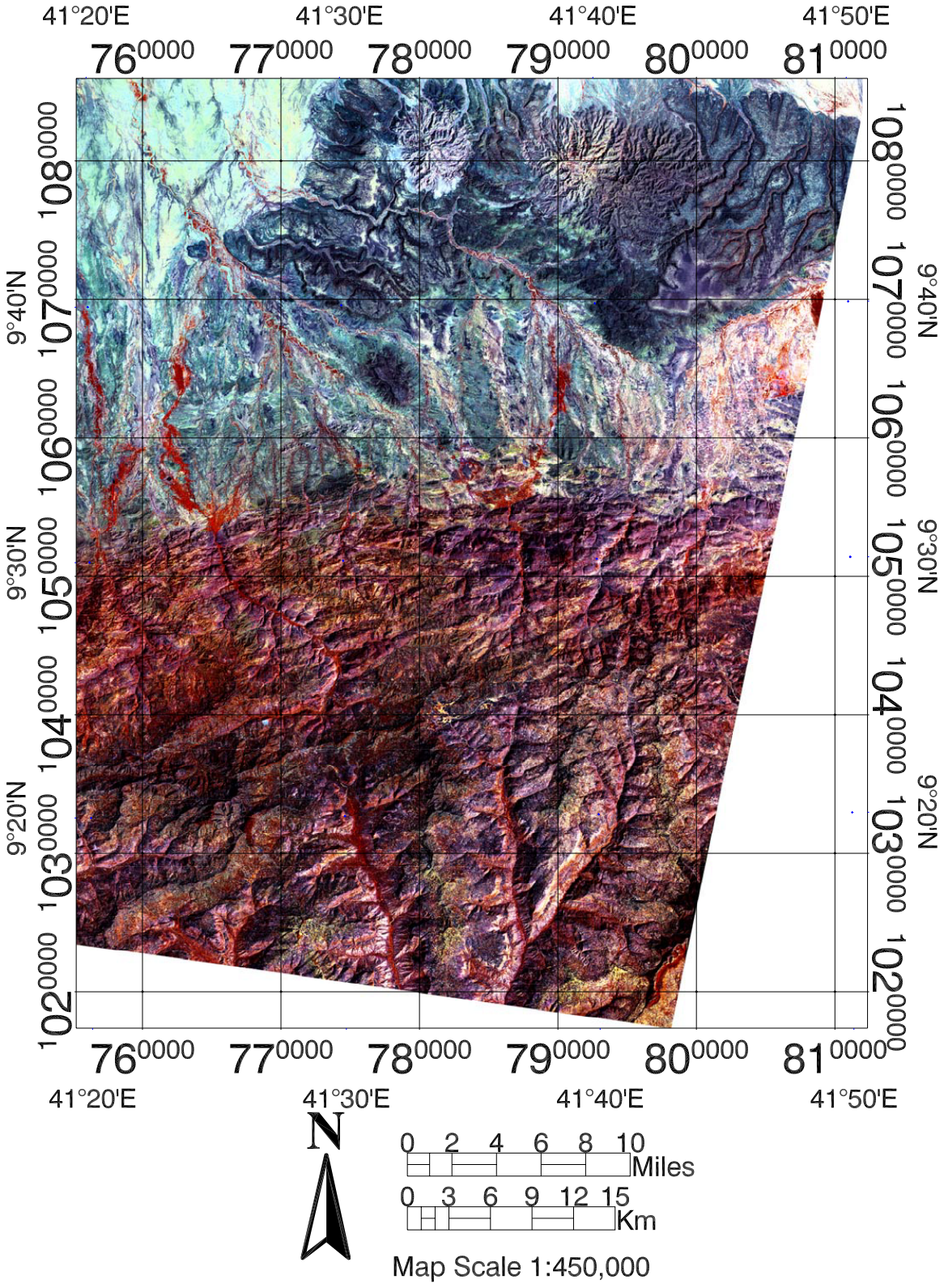
41°20'E
41°30'E
41°40'E
41°50'E
760000
770000
780000
790000
800000
810000
1080000
1070000
1060000
1050000
1040000
1030000
1020000
9°40'N
9°30'N
9°20'N
N
0 2 4 6 8 10
Miles
0 3 6 9 12 15
Km
Map Scale 1:450,000

Figure 12

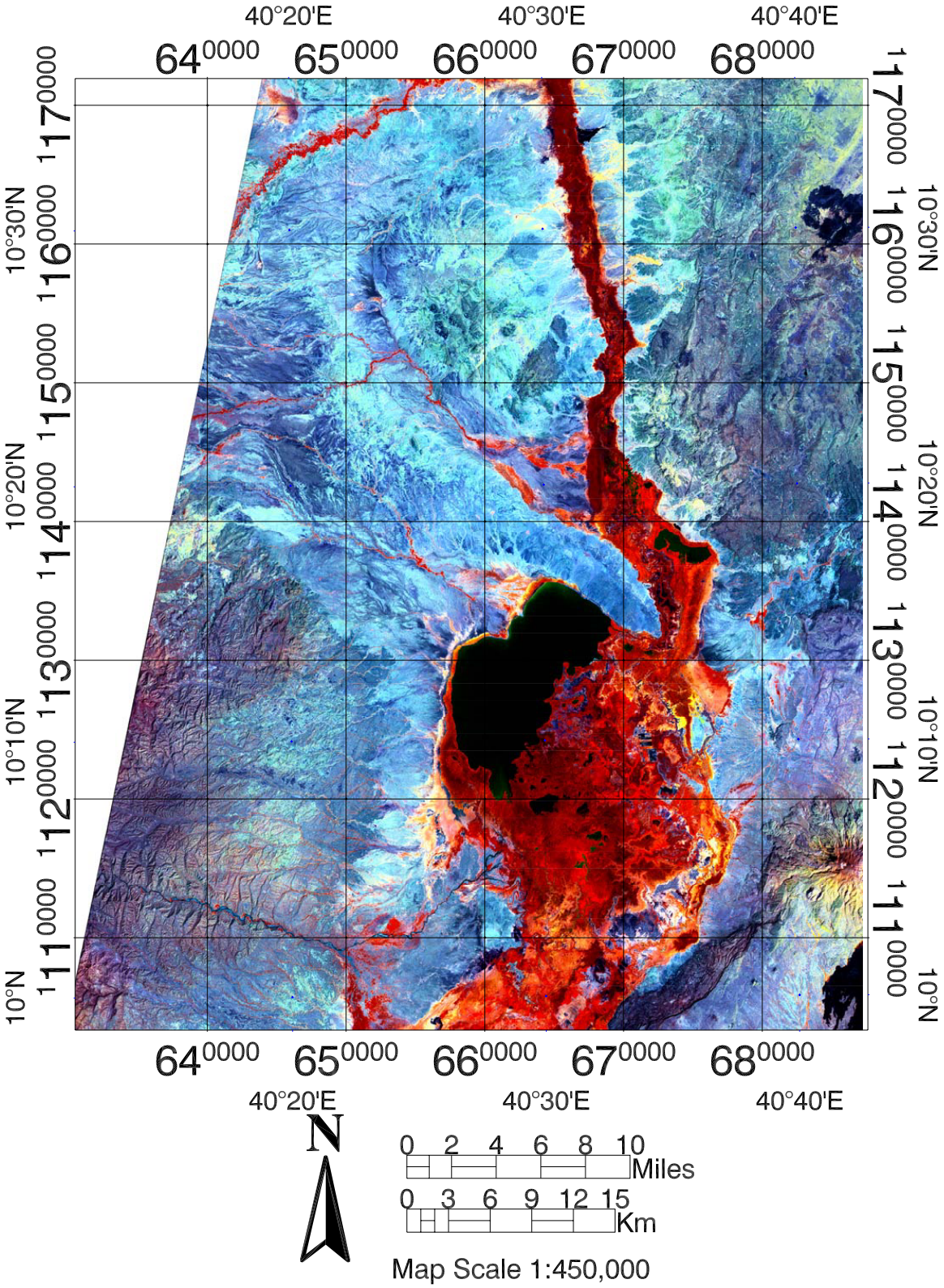
40°20'E
40°30'E
40°40'E
640000
650000
660000
670000
680000
1170000
1160000
1150000
1140000
1130000
1120000
1110000
10°30'N
10°20'N
10°10'N
10°N
N
0 2 4 6 8 10
Miles
0 3 6 9 12 15
Km
Map Scale 1:450,000

Figure 13

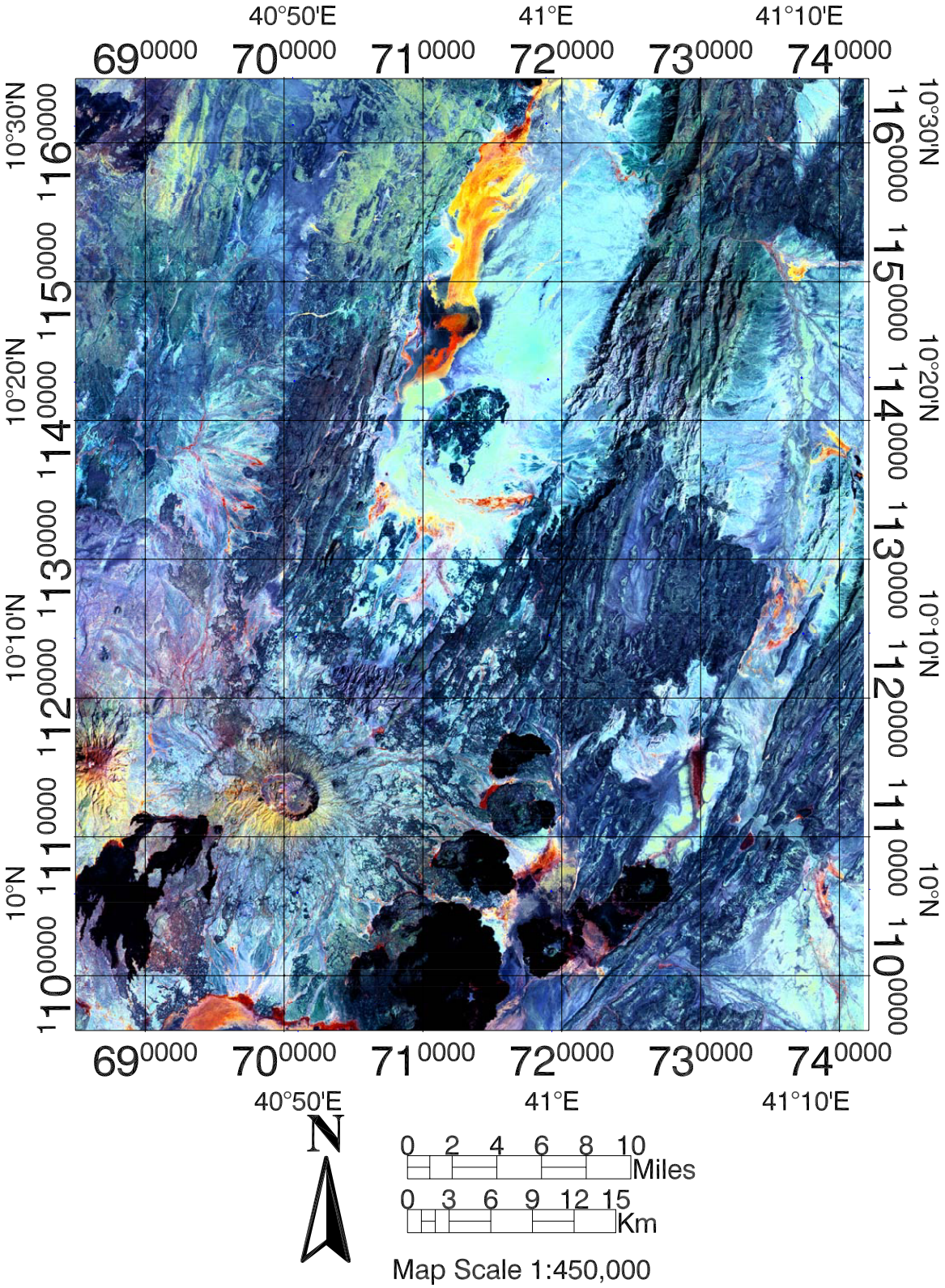
40°50'E
41°E
41°10'E
69 0000
70 0000
71 0000
72 0000
73 0000
74 0000
10°30'N
10°20'N
10°10'N
10°N
116 0000
115 0000
114 0000
113 0000
112 0000
111 0000
110 0000
N
0 2 4 6 8 10
Miles
0 3 6 9 12 15
Km
Map Scale 1:450,000

Figure 14

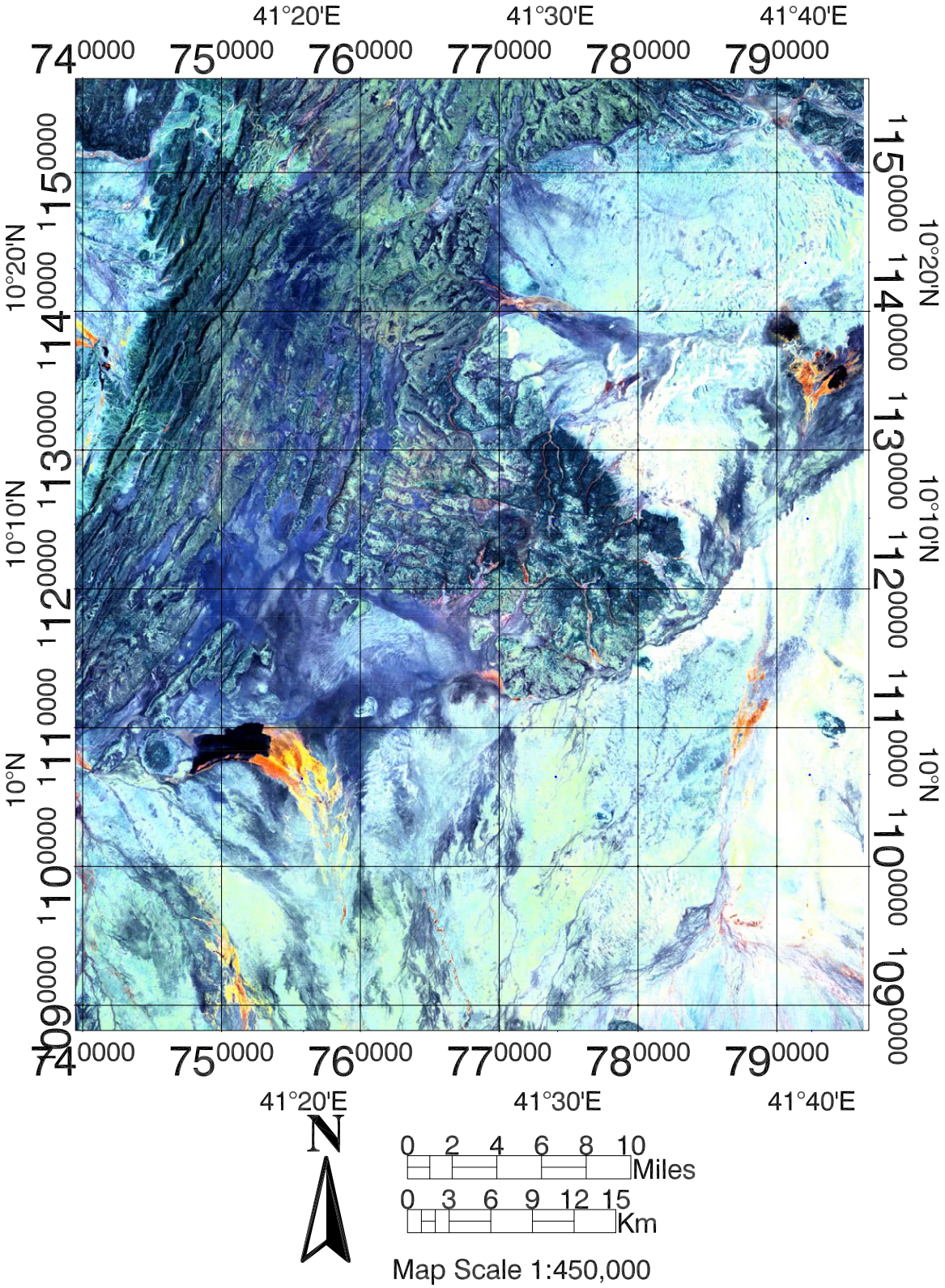
41°20'E
41°30'E
41°40'E
74 0000
75 0000
76 0000
77 0000
78 0000
79 0000
10°20'N
10°10'N
10°N
115 0000
114 0000
113 0000
112 0000
111 0000
110 0000
109 0000
N
0 2 4 6 8 10
Miles
0 3 6 9 12 15
Km
Map Scale 1:450,000

Figure 15

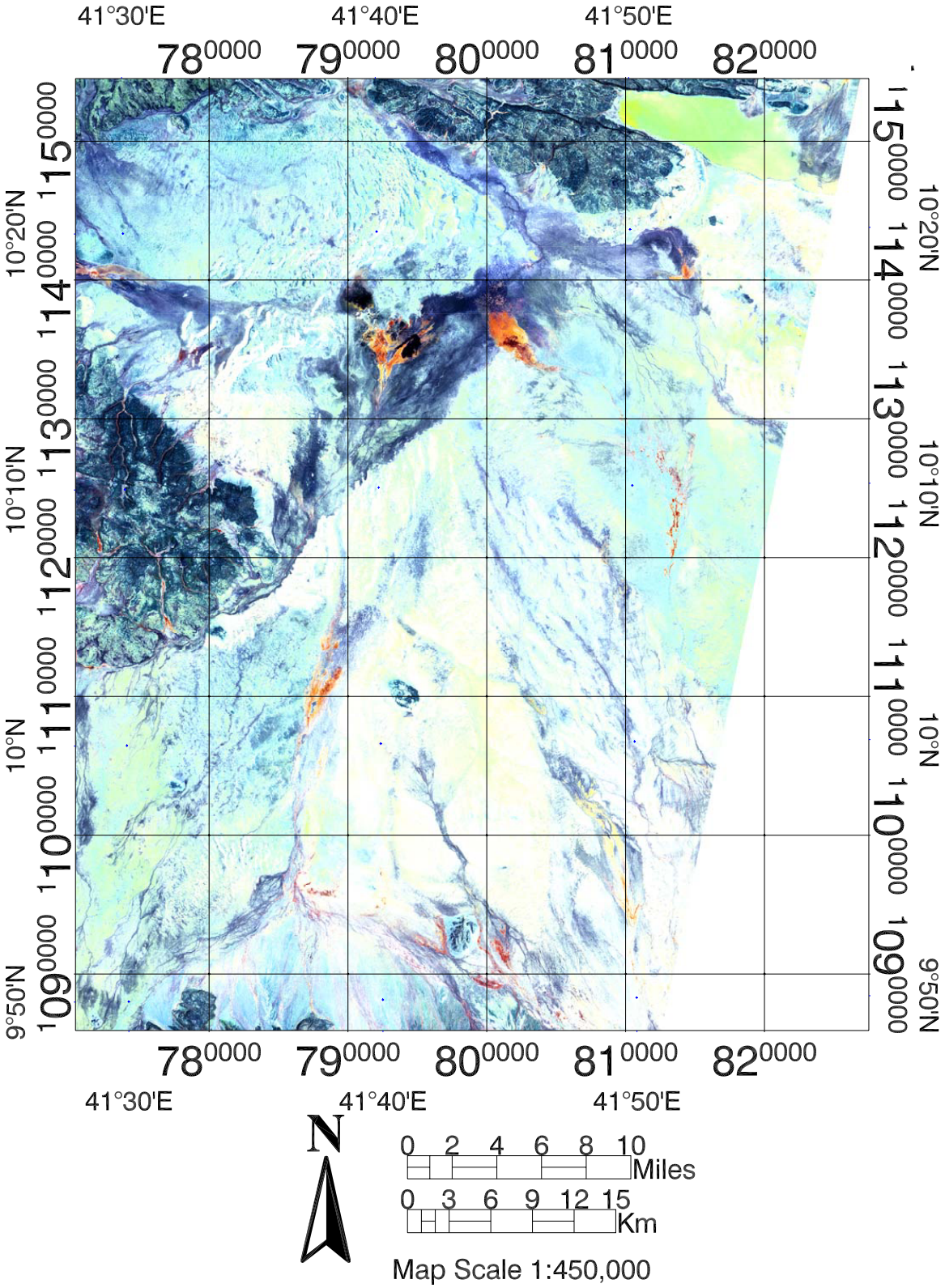
41°30'E
41°40'E
41°50'E
780000
790000
800000
810000
820000
10°20'N
10°10'N
10°N
9°50'N
1150000
1140000
1130000
1120000
1110000
1100000
1090000
N
0 2 4 6 8 10
Miles
0 3 6 9 12 15
Km
Map Scale 1:450,000

Figure 16

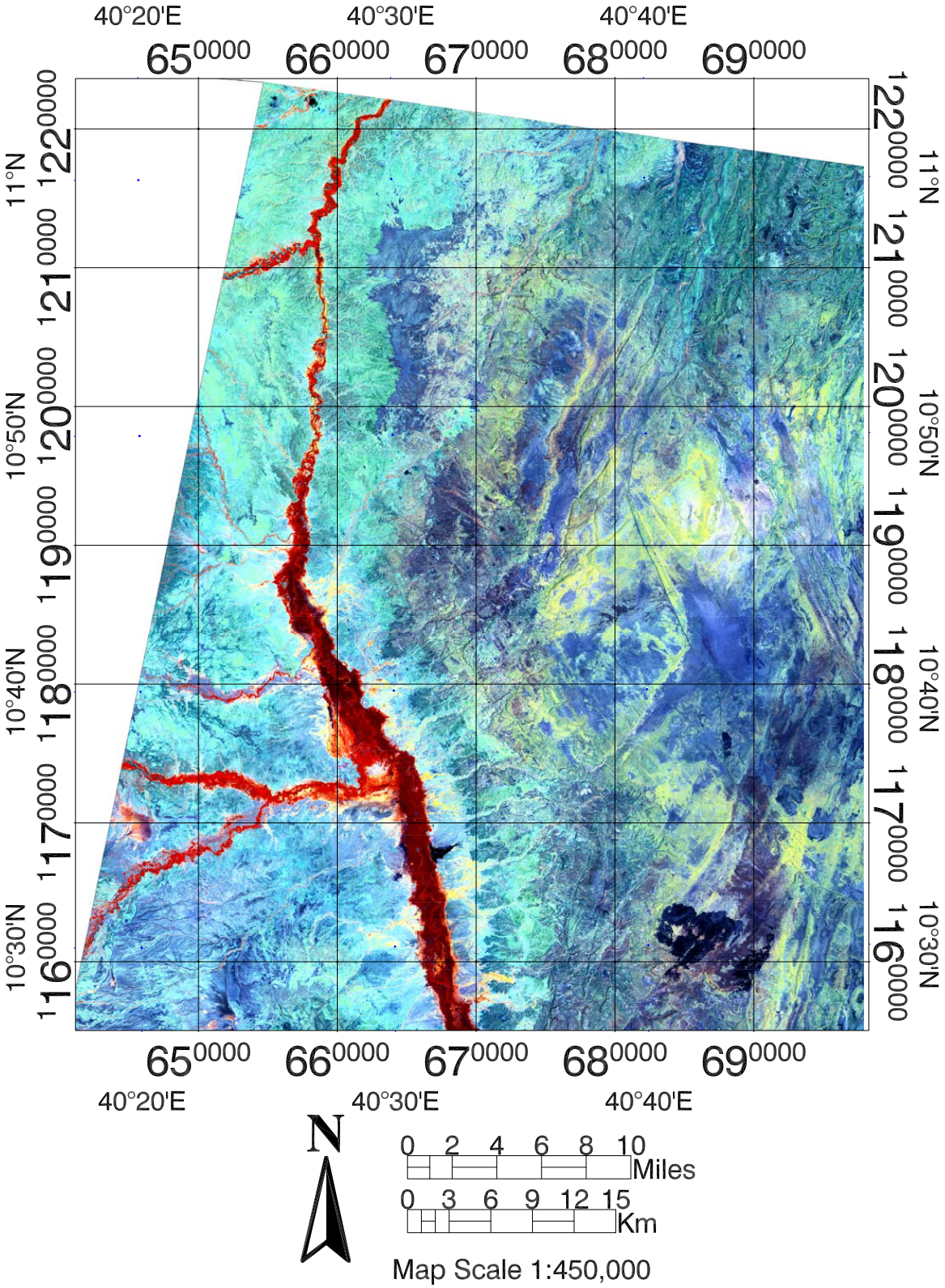
40°20'E
40°30'E
40°40'E
65 0000
66 0000
67 0000
68 0000
69 0000
122 0000
121 0000
120 0000
119 0000
118 0000
117 0000
116 0000
11°N
10°50'N
10°40'N
10°30'N
N
0 2 4 6 8 10
Miles
0 3 6 9 12 15
Km
Map Scale 1:450,000

Figure 17

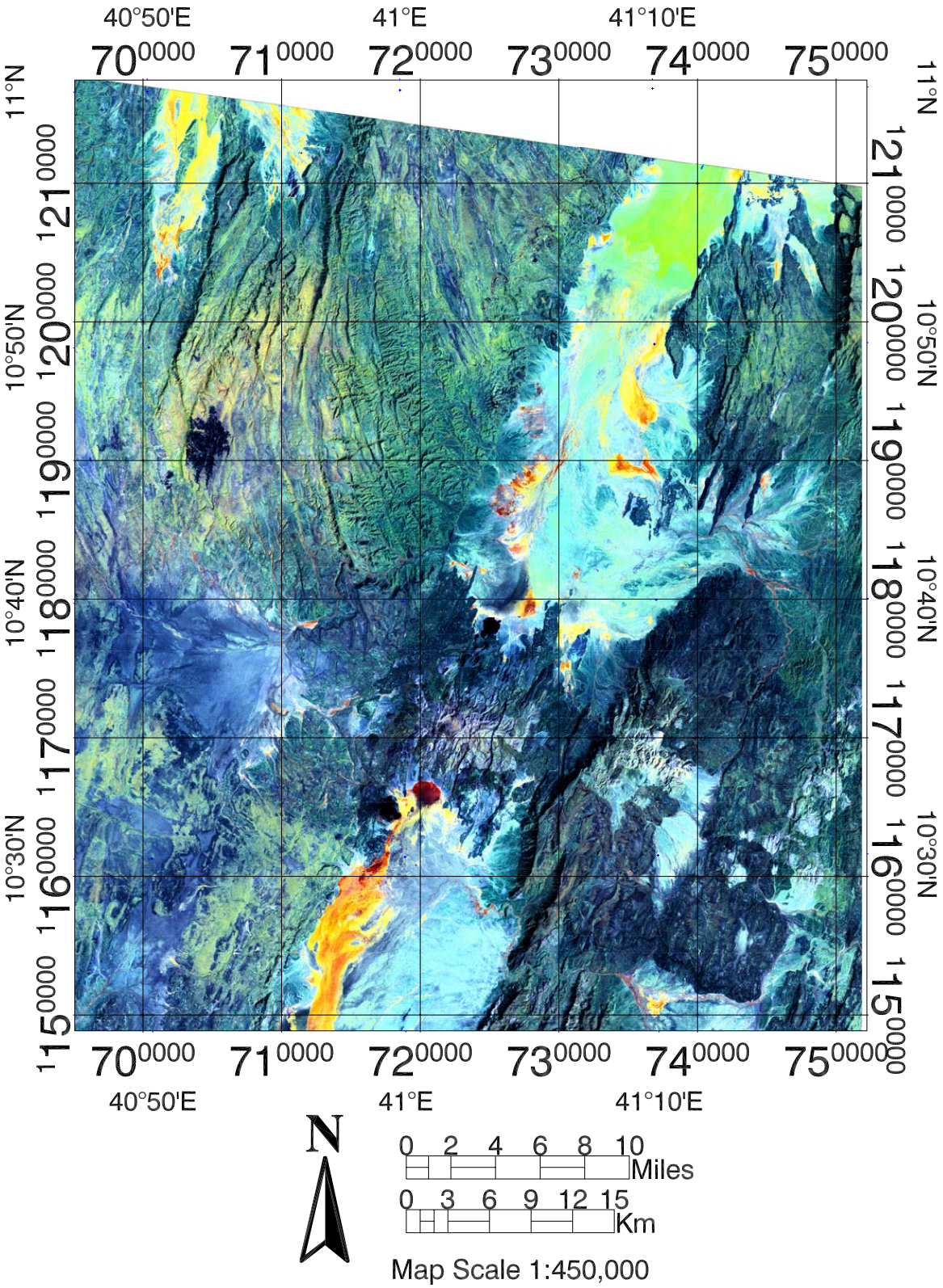
40°50'E
41°E
41°10'E
70 0000
71 0000
72 0000
73 0000
74 0000
75 0000
11°N
10°50'N
10°40'N
10°30'N
121 0000
120 0000
119 0000
118 0000
117 0000
116 0000
115 0000
N
0 2 4 6 8 10
Miles
0 3 6 9 12 15
Km
Map Scale 1:450,000

Figure 18

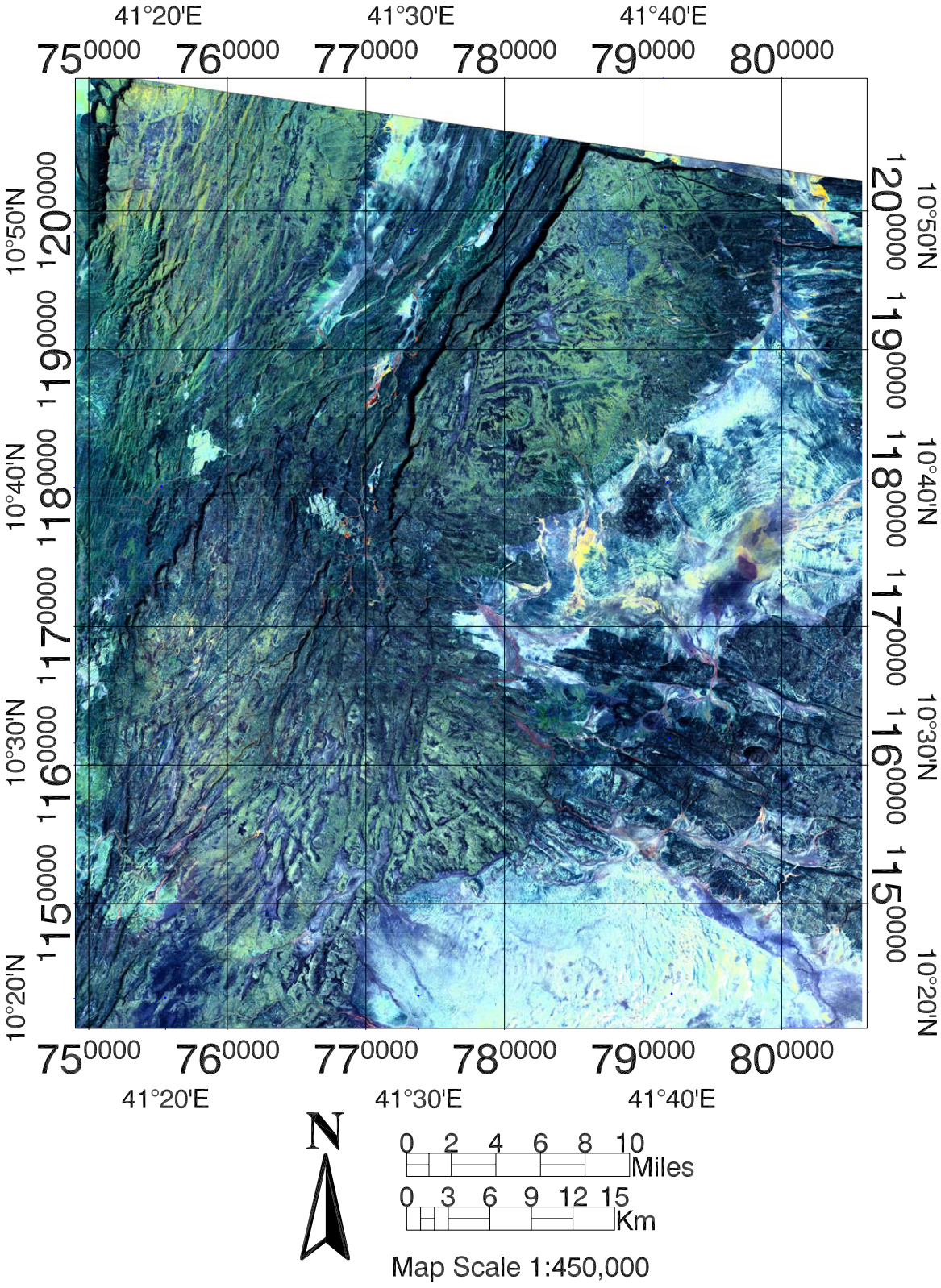
41°20'E
41°30'E
41°40'E
75 0000
76 0000
77 0000
78 0000
79 0000
80 0000
10°50'N
10°40'N
10°30'N
10°20'N
120 0000
119 0000
118 0000
117 0000
116 0000
115 0000
N
0 2 4 6 8 10 Miles
0 3 6 9 12 15 Km
Map Scale 1:450,000

Figure 19

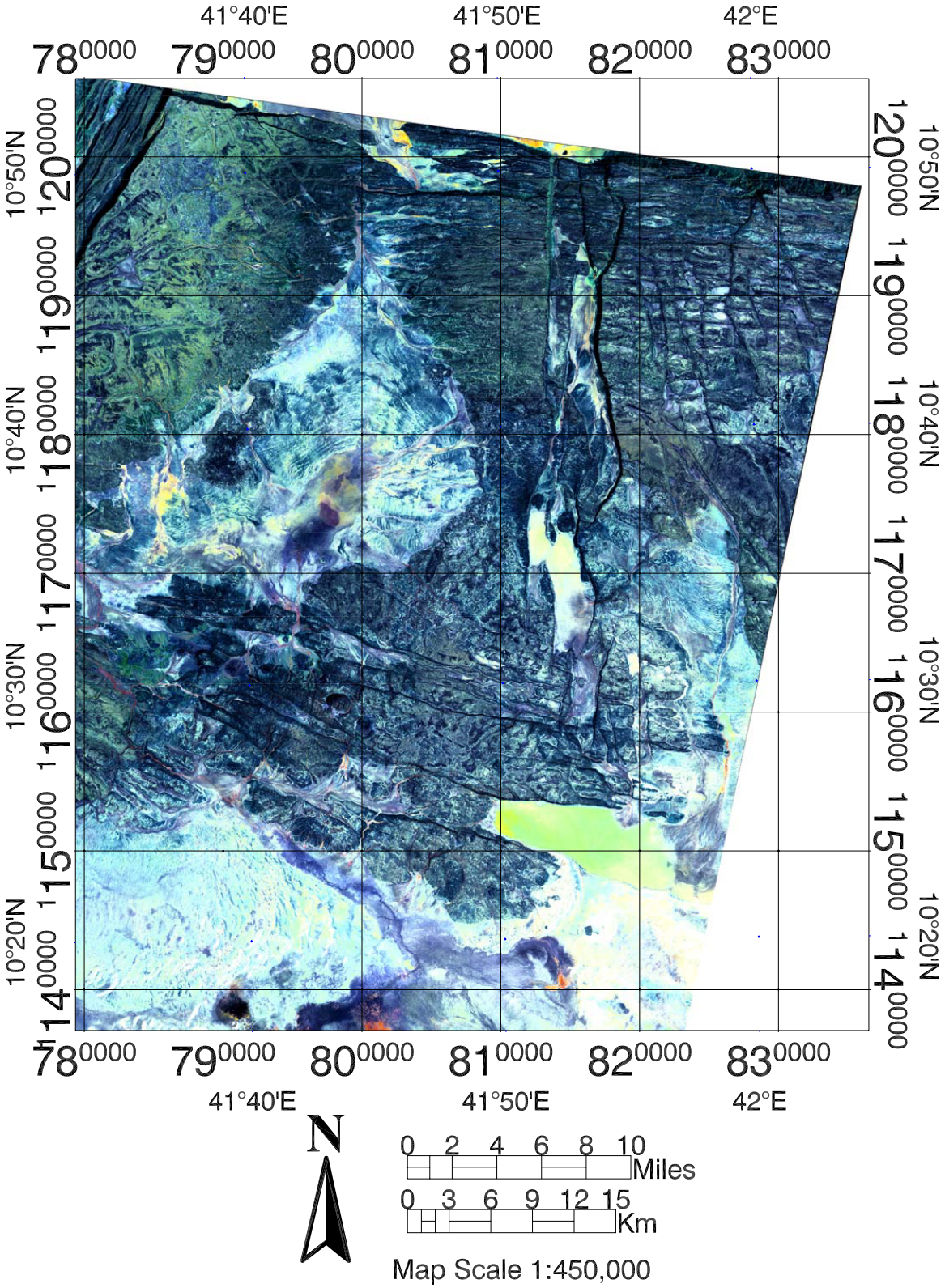
41°40'E
41°50'E
42°E
780000
790000
800000
810000
820000
830000
10°50'N
10°40'N
10°30'N
10°20'N
1200000
1190000
1180000
1170000
1160000
1150000
1140000
N
0 2 4 6 8 10
Miles
0 3 6 9 12 15
Km
Map Scale 1:450,000

Figure 20

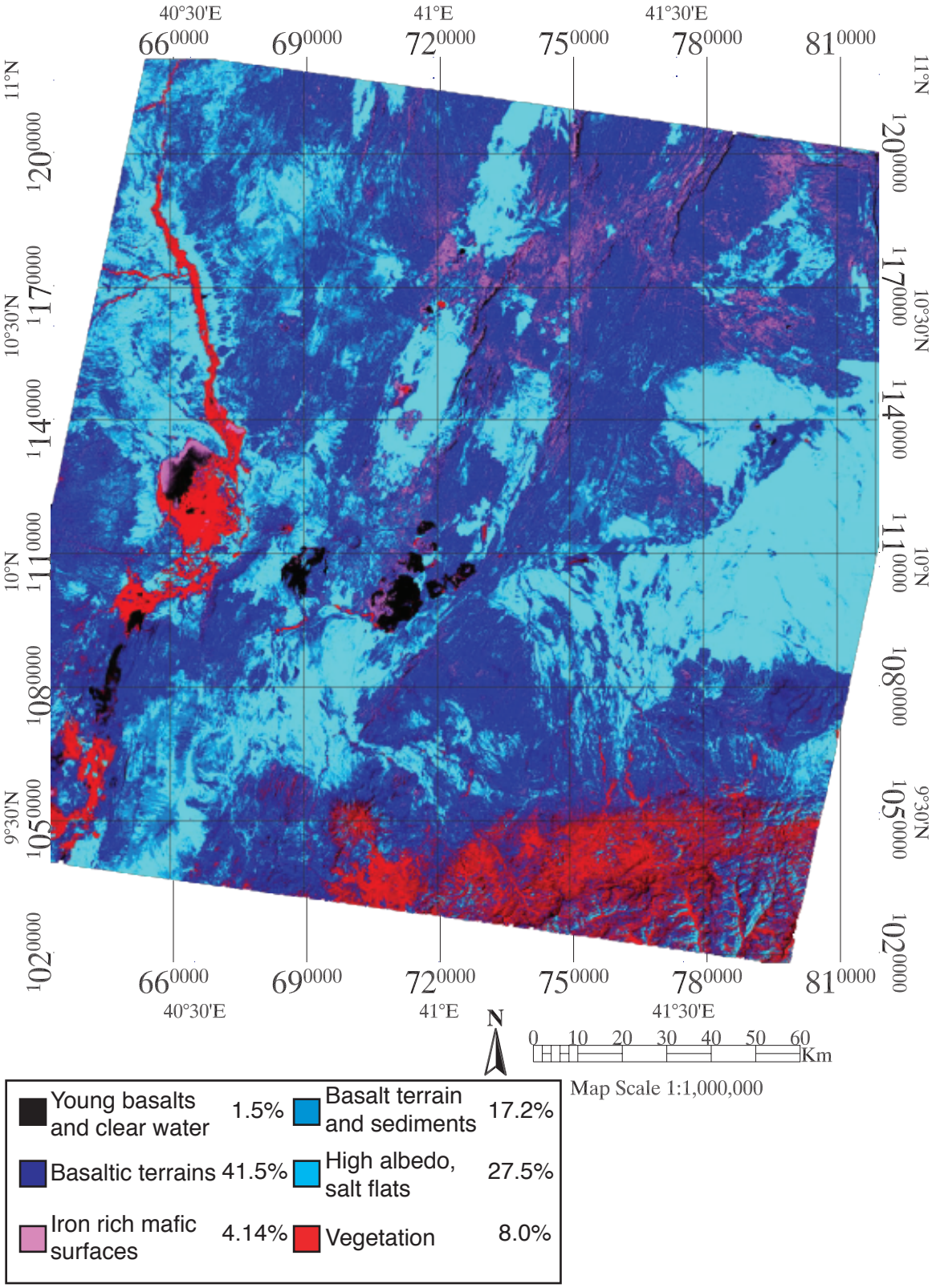

Figure 21- ISODATA terrain synopsis, with % coverage adjusted for missing edge data.